Geochemistry 85 (2025) 126287

Contents lists available at ScienceDirect

Geochemistry

journal homepage: www.elsevier.com/locate/chemer

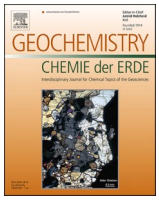

Permo-Triassic magmatism in the Damaraland Igneous Province, NW Namibia: The Ondurakorume alkaline-carbonatite complex☆

Andreja Ladisic [a,*], Michael A.W. Marks [a], Benjamin F. Walter [a], R. Johannes Giebel [b,c], Aratz Beranoaguirre [d,e], Gregor Markl [a]

[a] Eberhard Karls Universität Tübingen, Department of Geosciences, Scharrenbergstraße 94-96, 72072 Tübingen, Germany
[b] Technische Universität Berlin, Institute of Applied Geosciences, Ernst-Reuter-Platz 1, 10587 Berlin, Germany
[c] University of the Free State, Department of Geology, 250 Nelson-Mandela-Drive, Bloemfontein 9300, South Africa
[d] Goethe-University Frankfurt, Department of Geosciences, Altenhöferallee 1, 60438 Frankfurt, Germany
[e] Institute of Applied Geosciences, Karlsruhe Institute of Technology, Adenauerring 20a, 76131 Karlsruhe, Germany

ARTICLE INFO

Handling Editor: Tomas Magna

Keywords:
Mineral chemistry
U-Pb age dating
Wall rock interaction
Igneous petrology
Fenitization
Metasomatism
Silicocarbonatite

ABSTRACT

The four spatially associated igneous complexes of Kalkfeld, Ondurakorume, Osongombo and Etaneno are situated within the Damaraland Igneous Province (northwestern Namibia), which formed in response to the rifting of the South Atlantic during the early Cretaceous. Spatially-resolved LA-ICP MS U-Pb age dating on zircon and titanite confirms the Cretaceous age for Etaneno (mean of 139.2 ± 6.7 Ma), while Triassic and Permian emplacement ages are indicated for nepheline syenites from Kalkfeld (249.6 ± 3.2 and 249.4 ± 2.9 Ma) and Ondurakorume (272.1 ± 1.5 Ma). Furthermore, apatite ages for nepheline syenites from Etaneno (mean of 122.8 ± 3.8 Ma) and Kalkfeld (217.4 ± 24.5 Ma), and for carbonatites of Ondurakorume (248.1 ± 4.8 Ma) broadly agree with the zircon and titanite ages, while apatite from basement marbles yields a presumably metamorphic age of 479.6 ± 2.6 Ma and 465.1 ± 7.0 Ma.

Detailed petrographic analysis of syenites, nepheline syenites, carbonatites, silicocarbonatites and fenites from Ondurakorume reveals variable interaction processes between alkaline-silicate rocks and carbonatites. Syenites and nepheline syenites contain interstitial calcite with burbankite or carbocernaite inclusions (as commonly found in calcite carbonatites) and baddeleyite-zircon replacement textures. In some carbonatites and in silicocarbonatites, local contamination with (nepheline) syenites and granitic basement caused elevated Si activity, triggering enhanced formation of clinopyroxene, amphibole and mica.

Compositional variations in the released fenitizing fluids are indicated by clinopyroxene compositions that vary from nearly end-member aegirine ($Aeg_{69-91}Di_{0-10}Hed_{0-7}$) in proximal fenites to less sodic aegirine-augite ($Aeg_{54-96}Di_{0-17}Hed_{0-16}$) in more distal fenite samples, with the latter containing additional sodic amphibole. Compared to clinopyroxene in nepheline syenites and carbonatites, clinopyroxene in fenites shows elevated Ti contents (mostly >0.05 apfu Ti) that are highest in distal fenites (up to 0.22 apfu Ti), suggesting Ti mobility. These changes suggest either a compositional evolution during fluid-rock interaction or two different fluid sources (carbonatites and (nepheline) syenites, respectively).

1. Introduction

Carbonatites are magmatic rocks with >50 % modal carbonates and <20 wt% SiO_2, if they contain >20 wt% SiO_2, they are classified as silicocarbonatites (Le Maitre et al., 2002; Mitchell, 2005). Depending on the dominant carbonate mineral, they are subdivided into calcite, dolomite, ferro- (ankerite, siderite), and natrocarbonatites (nyerereite, gregoryite). Most carbonatites are associated with various ultramafic (e.g. pyroxenite, dunite, peridotite) and evolved alkaline silicate rocks (e.g. syenite, ijolite, foidolite; Woolley and Kjarsgaard, 2008) and such alkaline-carbonatite complexes carry an economic potential as they are often enriched in commodities, such as rare earth elements (REE, usually

☆ This article is part of a Special issue entitled: 'News in carbonatite world' published in Geochemistry.

* Corresponding author.
E-mail addresses: andreja.ladisic@uni-tuebingen.de (A. Ladisic), michael.marks@uni-tuebingen.de (M.A.W. Marks), benjamin.walter@uni-tuebingen.de (B.F. Walter), r.j.giebel@tu-berlin.de (R.J. Giebel), beranoaguirre@em.uni-frankfurt.de (A. Beranoaguirre), markl@uni-tuebingen.de (G. Markl).

https://doi.org/10.1016/j.chemer.2025.126287
Received 24 July 2024; Received in revised form 5 February 2025; Accepted 26 March 2025
Available online 27 March 2025

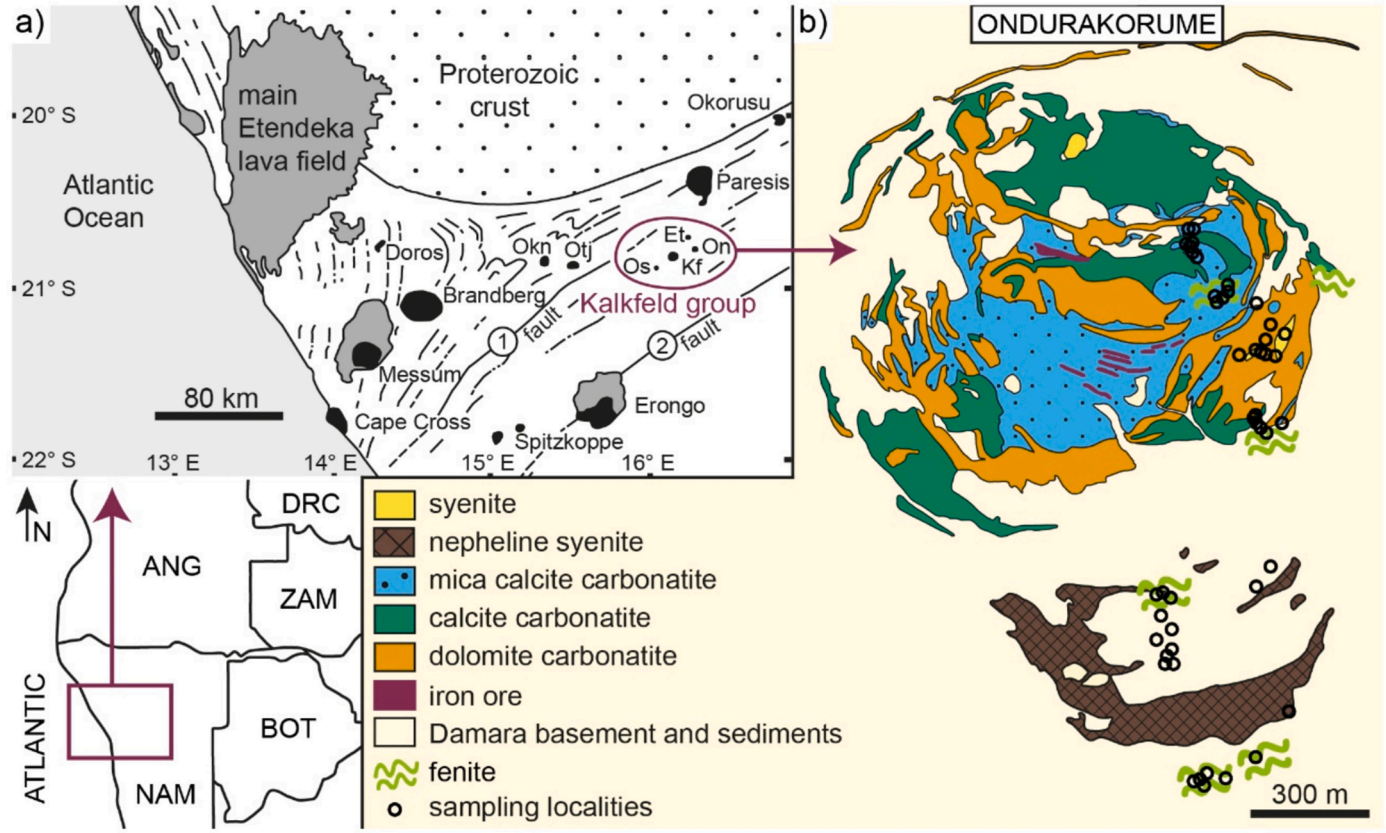

Fig. 1. a) A sketch of Damaraland Igneous Province in NW Namibia representing granitic, alkaline and carbonatitic complexes in black (Okn – Okenyenya, Otj – Otjihorongo), Etendeka volcanics in grey, and the circled study area – the Kalkfeld group (Kf – Kalkfeld, On – Ondurakorume, Et – Etaneno, Os – Osongombo), located between Autseib Fault-Otjihorongo Thrust (1) and Omaruru Lineament-Waterberg Thrust (2). The sketch was taken from Kramm et al. (2017), and was slightly modified. b) Simplified geological map of Ondurakorume carbonatite complex after Prins (1978), additionally showing locations of samples investigated in this study marked with black empty circles, and locations of found fenites.

LREE La—Sm), high field strength elements (HFSE, e.g. Ti, Zr, Nb, U), as well as Sr, P, Ba and others (Nelson et al., 1988; Chakhmouradian, 2006; Anenburg et al., 2021). Although a magmatic origin for most carbonatites has been widely accepted, the exact process behind their formation remains a subject of ongoing debate. Three hypotheses are most commonly described for their genesis: (1) residual magmas derived by fractionation of CO_2-bearing nephelinitic to melilititic melts; (2) immiscible melt fractions of CO_2-saturated silicate melts; and (3) primary mantle melts generated through partial melting of CO_2-bearing peridotite or eclogite (Jones et al., 2013; Yaxley et al., 2022; Gittins and Mitchell, 2023).

The emplacement of carbonatites is often accompanied by fenitization, a process in which alkali- and solvent-rich fluids/brines expelled from the crystallization and cooling of the carbonatite magma metasomatize the surrounding wall rocks (Le Bas, 2008; Elliott et al., 2018; Walter et al., 2021). Common minerals in fenites are albite, orthoclase, mica, sodic clinopyroxene (e.g. aegirine), and sodic amphibole (e.g. arfvedsonite, riebeckite), which crystallize along grain boundaries or in fractures produced by pressure release of crystallizing carbonatite (Le Bas, 2008; Elliott et al., 2018).

In recent years, there has been a renewed interest in the direct interaction of carbonatite magma and wall rocks, and in the potential for contamination of carbonatite magmas during crustal emplacement. Recent experimental work of Anenburg and Mavrogenes (2018) introduced the term “antiskarn” for rocks which form by such interaction, where the exchange primarily of Si, Al, Ca, Mg, and Fe happens. While still under debate, additional experimental work (Vasyukova et al., 2022; Anenburg and Walters, 2024), as well as field evidence (Giebel et al., 2019; Bouabdellah et al., 2022; Vasyukova and Williams-Jones, 2022; Voropaeva et al., 2024) highlighted the significance of carbonatite magma – silicate wall rock interaction as an important process in carbonatite genesis.

The study area for this contribution is the so-called Kalkfeld Group in northwestern Namibia, which consist of four spatially associated alkaline-carbonatitic magmatic centres: the Kalkfeld complex (featuring a central carbonatite which is sometimes referred to as “Eisenberg”), Ondurakorume (Kameelberg), Etaneno and Osongombo (Verwoerd, 1967). A special emphasis is put on the petrology of Ondurakorume for this study, as the carbonatites were not described in sufficient detail in relation to the silicate rocks and the surrounding fenites. Updated and detailed descriptions of the distinct carbonatite lithologies and the associated alkaline silicate rocks, fenites and silicocarbonatites are provided, including new mineral chemistry data for apatite, clinopyroxene, and mica. Moreover, the new in-situ U-Pb age data (apatite, titanite and zircon) are compared with recent age data for Kalkfeld and Ondurakorume (Kramm et al., 2017; Sun et al., 2024). Although having similar lithologies and being spatially associated, the ages indicate that, unlike Etaneno, the Ondurakorume and Kalkfeld complexes are genetically unrelated to the Early Cretaceous complexes of the Damaraland Igneous Province (Comin-Chiaramonti et al., 2011). They rather indicate an older alkaline-carbonatite magmatic event that was emplaced by the reuse of existing, deep-reaching structures.

2. Geological setting

Northwestern Namibia consists of Paleo- and Mesoproterozoic gneisses, metasediments, and metavolcanics, overlain by rocks of the Damara Belt, which represents a NE-SW trending arm of the

Neoproterozoic Pan-African Damara Orogen that extends across central Namibia. This unit consists of metasediments (marbles, quartzites, schists) intruded by granitic, granodioritic, dioritic, and gabbroic plutons of 550–460 Ma in age (Miller, 2008; Toé et al., 2013). Much later and coinciding with the breakup of Gondwana during the Early Cretaceous, large volumes of basalts and silicic volcanics where erupted on both sides of the South Atlantic rift, forming the well-known Paraná-Etendeka Large Igneous Province (Gomes and Vasconcelos, 2021). On the Namibian side, about 20 igneous centres were emplaced along NE-SW trending main crustal discontinuities, stretching inland for about 350 km (Miller, 2008). These complexes have variable compositions, including ultramafic rocks, gabbros, granites, syenites, and carbonatites and form the so-called Damaraland Igneous Province (DIP; Fig. 1a).

As for the Paraná-Etendeka volcanism, the cause from magmatism of the DIP is generally seen in the activity of the Tristan mantle plume, interacting with a heterogeneous sub-continental mantle and the crust, producing lithologically and geochemically diverse magmatism (e.g., Milner et al., 1995; Le Roex and Lanyon, 1998; Trumbull et al., 2000, 2003; Ewart et al., 2004; Comin-Chiaramonti et al., 2007; Gomes et al., 2018). Indeed, high-precision ages for the DIP complexes are around 133 Ma (Sun et al., 2024), just around or shortly after the peak of the volcanic activity of Paraná-Etendeka volcanism (135–133 Ma, Gomes and Vasconcelos, 2021).

The magmatic centers of Etaneno, Kalkfeld, Osongombo and Ondurakorume (the Kalkfeld group) in the DIP belong to the north Central Zone (nCZ) located between two major shear zones (Autseib Fault and Omaruru Lineament). They are spatially closely associated with each other (Fig. 1a) and consist of variable evolved and mostly felsic alkaline rocks (mostly syenites, foid syenites and phonolites), dyke rocks and carbonatites. Following first basic descriptions (Verwoerd, 1967; Verwoerd et al., 2000; Prins, 1978), they have been investigated using modern techniques (Le Roex and Lanyon, 1998; Bühn et al., 2001; Bühn and Trumbull, 2003; Bühn, 2008). However, no petrological studies for Osongombo exist but the one of Prins (1978). Recent work of Kramm et al. (2017) and Sun et al. (2024) determined Permo-Triassic ages for Kalkfeld (~242 Ma) and Ondurakorume (~275 Ma), which required a reevaluation of the geodynamic cause for some of the magmatic centers, assumed to be part of the DIP. The prime focus of this contribution, however, lies on the insufficiently studied Ondurakorume complex, which is described in some detail in the following.

2.1. *The Ondurakorume carbonatite complex*

The Ondurakorume carbonatite complex, also called Kameelberg (Fig. 1b), is an approximately 1.4 km wide circular composite intrusive complex that elevates to a height of about 275 m above the Damaraland plain. The southern area is composed of nepheline syenites, separated by country rocks from the northern part, where different varieties of carbonatites intruded in a concentric manner into basement rocks of the Damara Belt. Calcite carbonatite forms five major bodies and several smaller ones around a central, mica calcite carbonatite intrusion. Dolomite carbonatite ring dykes intruded mainly along the contact between mica- and calcite carbonatites, and along the outer margin of the complex. At the present erosion level, intrusion breccias made of clastic country rocks set in a carbonatitic matrix are found only sporadically. Carbonatites host several syenite rafts and mega-xenoliths that reach up to ten meters in diameter. These rafts and mega-xenoliths are a part of an approximately 300 m wide fenite halo which metasomatized the Damara basement rocks and nepheline syenites. The fenites are commonly identified by green sodic clinopyroxene, sodic amphibole, and altered alkali feldspar. Towards the top of the complex, carbonatites are overlain by weathered Fe-rich crusts which can reach up to 10 m of thickness, and can sporadically consist of euhedral and up to one centimeter sized magnetite crystals.

Table 1
Thin section samples from Ondurakorume carbonatite complex with their coordinates and determined lithology.

NUMBER	SAMPLE ID	UTM COORDINATES	LITHOLOGY
1	ON001	33K 631304 7703115	dolomite carbonatite dyke
2	ON002	33K 631296 7703113	carbonatite breccia
3	ON005	33K 631290 7703068	dolomite-b. calcite carbonatite
4	ON006	33K 631287 7703048	dolomite-b. apatite calcite carbonatite
5	ON007	33K 631299 7703038	dolomite-b. apatite calcite carbonatite
6	ON010A	33K 631415 7702976	dolomite-b. calcite carbonatite dyke
7	ON010B	33K 631415 7702976	fenitized syenite
8	ON017	33K 631547 7702800	dolomite carbonatite dyke
9	ON019	33K 631516 7702804	apatite calcite carbonatite dyke
10	ON021	33K 631585 7702799	apatite-b. calcite carbonatite
11	ON022A	33K 631615 7702860	dolomite carbonatite dyke
12	ON023	33K 631611 7702627	fenitized (nepheline) syenite
13	ON027	33K 631549 7702609	silicocarbonatite
14	ON028	33K 631575 7702598	amphibole-b. dolomite carbonatite dyke
15	ON029	33K 631163 7701330	fenitized granite
16	ON030	33K 631208 7701351	calcite carbonatite dyke
17	ON031	33K 631156 7701348	calcite carbonatite dyke and fenite contact
18	ON033	33K 631264 7701399	fenitized (nepheline) syenite
19	ON036	33K 631369 7701982	apatite-b. calcite carbonatite
20	ON037	33K 631315 7701916	syenite
21	ON038	33K 631027 7701851	apatite-b. calcite carbonatite
22	ON039	33K 631013 7701857	syenite
23	ON041	33K 631001 7701786	nepheline syenite
24	ON045	33K 631019 7701656	nepheline syenite
25	ON046	33K 631004 7701662	nepheline syenite
26	ON047	33K 630982 7701707	nepheline syenite

Note. b. – bearing.

3. Sample material and analytical methods

The studied samples were collected during fieldwork in 2021, and after careful evaluation of the different lithologies, their mineralogy and textures, 26 samples from Ondurakorume were chosen for further analytical work. The sample set comprises 15 carbonatites, six (nepheline) syenites, five fenitized rocks and only one breccia (note that sample ON031 is counted twice because it is a contact between the carbonatite and the fenite; Table 1).

For comparative age-dating purposes, samples from Kalkfeld ($n = 2$), Etaneno ($n = 4$), and Osongombo ($n = 1$) were added to samples from Ondurakorume ($n = 3$) (Table 2). Polished thin-sections were investigated using transmitted-light microscopy (Leica DM750P and Leica Laborlux 12POLS), photomicrographs were taken with an Olympus EM5II and Nikon COOLPIX 950 digital cameras attached respectively to

Table 2
The Kalkfeld group samples chosen for U-Pb age dating with their coordinates, major, minor and accessory phases.

NUMBER	SAMPLE ID	UTM COORDINATE	MAJOR	MINOR	ACCESSORY
1	ON021	33K 631585 7702799	ap, cal	–	anc-Ce, bbn/ cbc, bt, clb-Fe, cpx, mag, mnz-Ce, pcl, zrn
2	ON041	33K 631001 7701786	afs, ccn, mag	bt, nph, cpx	ap, cal, pcl, zrn
3	ON046	33K 631004 7701662	afs, ccn, nph, cpx	bt, mag	ap, cal, pcl, ttn, zrn
4	KF037	33K 618144 7695698	afs, nph	bt, mag	ap, ccn, cpx, ttn
5	KF048	33K 615647 7695425	afs, bt, nph, cpx	mag	ap, cal, ccn, ttn
6	ET001	33K 625248 7710314	afs, nph, cpx	amp, bt, mag, ol	ap, sdl, zrn
7	ET011	33K 625632 7710340	afs, amp, cpx	mag	ap, cal, pcl, sdl, zrn
8	ET019	33K 625838 7710322	afs, amp, nph, cpx	mag, ol	ap, bt, sdl, zrn
9	ET035	33K 626141 7709655	afs, mag, nph	cpx	amp, ap, pcl, sdl, ttn, zrn
10	OS006	33K 605351 7689902	cal, ank	–	ap, bt, dol, brt, hem, mag, pcl, sp, qz
11	OS019	33K 605037 7690323	cal	–	afs, brt, cpx, dol, flr, phl, py, zrn

Note. Abbreviations used: ap – apatite, cal – calcite, anc-Ce – ancylite-(Ce), bbn – burbankite, cbc – carbocernaite, bt – biotite, clb-Fe – columbite-(Fe), cpx – clinopyroxene, mag – magnetite, mnz-Ce – monazite-(Ce), pcl – pyrochlore, zrn – zircon, afs – alkali feldspar, ccn – cancrinite, nph – nepheline, ttn – titanite, amp – amphibole, ol – olivine, sdl – sodalite, ank – ankerite, sp – sphalerite, dol – dolomite, brt – baryte, hem – hematite, qz – quartz, flr – fluorite, phl – phlogopite, py - pyrite.

the microscopes, and further documentation of the micro textures was done with a Tabletop Phenom XL SEM using BSE mode with a focused beam and an acceleration voltage of 15 kV on medium and low vacuum (10 Pa and 60 Pa) on carbon coated samples. A “hot cathode” cathodoluminescence (CL) microscope (lumic HC6-LM SG) with an Olympus XC10 camera was used with an acceleration voltage of ~14 kV and a beam current density of 9 μAmm^{-2} on the sample surface.

3.1. Electron microprobe analyses

For the Ondurakorume samples, compositional data for clinopyroxene, apatite, mica and amphibole were obtained using a JEOL JXA-8230 at University of Tübingen. The standards used were albite (Na), corundum (Al), diopside (Mg, Si, Ca), sanidine (K), Cr metal (Cr), zirconium dioxide (Zr), bustamite (Mn), $SrTiO_3$ (Sr, Ti), hematite (Fe), topaz (F), Durango apatite (Ca, F), LREE glasses (La, Ce, Pr, Nd), tugtupite (Cl), baryte (Ba, S), sanidine (K) and uranium dioxide (U). An acceleration voltage of 15 kV was used for all minerals, a beam current of 20 nA was used for clinopyroxene, mica and amphibole, and one of 10 nA for apatite. For apatite, Pr—La and F—Ce corrections had to be applied, and F—Fe correction for mica and amphibole. To minimize migration of Na and F during analysis, a 10 μm beam was used on apatite and a 5 or 10 μm beam for mica and amphibole, depending on the size of the mineral grain and homogeneous surface area. Peak counting times were 16 s for major elements and 30 s for trace elements, with background counting times half of the peak counting times. Used standards with respective diffraction crystals, as well as analysis conditions for each measured mineral can be found in Supplementary File 1, and all analysis points with mineral formulae and end-member calculations in Supplementary File 2.

3.2. U-Pb age dating via LA-SF-ICPMS

The U-Pb age data of zircon, titanite and apatite was collected on a ThermoFisher Element XR sector field ICPMS coupled to a 193-nm ArF Excimer laser with a HelEx 2-volume cell (Analyte Excite+, Teledyne PhotonMachines) at the Laboratory for Environmental and Raw Materials Analysis (LERA), Karlsruhe Institute of Technology (Germany), using a slightly modified method as previously described in Beranoaguirre et al. (2022). The data were acquired in three analytical sessions during June 2023. Information regarding the analytical parameters (spot size, repetition rate, acquisition times, gas flows, etc.) is detailed in Supplementary File 3. The $^{207}Pb/^{206}Pb$ and $^{206}Pb/^{238}U$ ratios were corrected for mass bias, including drift over time, using the primary reference materials GJ1 zircon (Jackson et al., 2004) in the first session, or NIST SRM 612 glass (Jochum et al., 2011) in the second and third sessions. In the case of apatite and titanite, an additional correction was applied to the $^{206}Pb/^{238}U$ ratios to account for compositional differences between the primary reference material and unknowns. This was done using Durango apatite (McDowell et al., 2005) and Khan titanite (Mazoz et al., 2022). Accuracy was verified by multiple analyses of a secondary reference zircon BB (Santos et al., 2017) and Plešovice (Sláma et al., 2008), Sumé apatite (Lana et al., 2021) and Bear Lake titanite (Mazoz et al., 2022). Data processing has been carried out using an in-house VBA Microsoft Excel© spreadsheet program (Gerdes and Zeh, 2006, 2009), which is based on Isoplot algorithms (Ludwig, 2012). Uncertainties are the quadratic addition of internal uncertainties, counting statistics, background, and the excess of scatter and variance (Horstwood et al., 2016).

4. Results

4.1. Petrography

The main lithological units of Ondurakorume are syenites, nepheline syenites, calcite carbonatites and dolomite carbonatites, as well as fenitized rocks and silicocarbonatites (Table 1).

4.1.1. Syenites

Syenites (samples ON037, ON039) are primarily made of subhedral alkali feldspar (up to 5 mm) with minor amounts of nepheline crystals (up to 2 mm), biotite (up to 1.8 mm) and interstitial calcite. Accessory phases include zircon (up to 1 mm), pyrochlore (up to 0.7 mm) and apatite (up to 0.8 mm) (Fig. 2a, b). Pyrochlore is mostly subhedral with rounded edges, cracked, and is in cases compositionally zoned. Zircon also forms subhedral crystals with cracked and corroded surfaces. Apatite is subhedral and often rounded, and shows oscillatory zoning when using CL. The cores are violet blue, followed by a slim reddish zone, which is not always present, and a third very light violet zone, that occasionally forms small patches in the core (Fig. 2b). Euhedral to subhedral alkali feldspar is perthitically exsolved and often forms twins (Fig. 2a), with sporadic small amounts of albite at the rims. Subhedral nepheline is commonly altered to zeolites and sericite, and shows small-scale replacement by cancrinite, particularly at the contact with calcite (Fig. 2a). Biotite contains small inclusions of iron oxide, typically a few tens of μm in size. Interstitial calcite contains inclusions of burbankite or carbocernaite and strontioburbankite (Fig. 2c).

4.1.2. Nepheline syenites

Nepheline syenites (samples ON041, ON045, ON046, ON047) are coarser grained than syenites and dominated by euhedral alkali feldspar

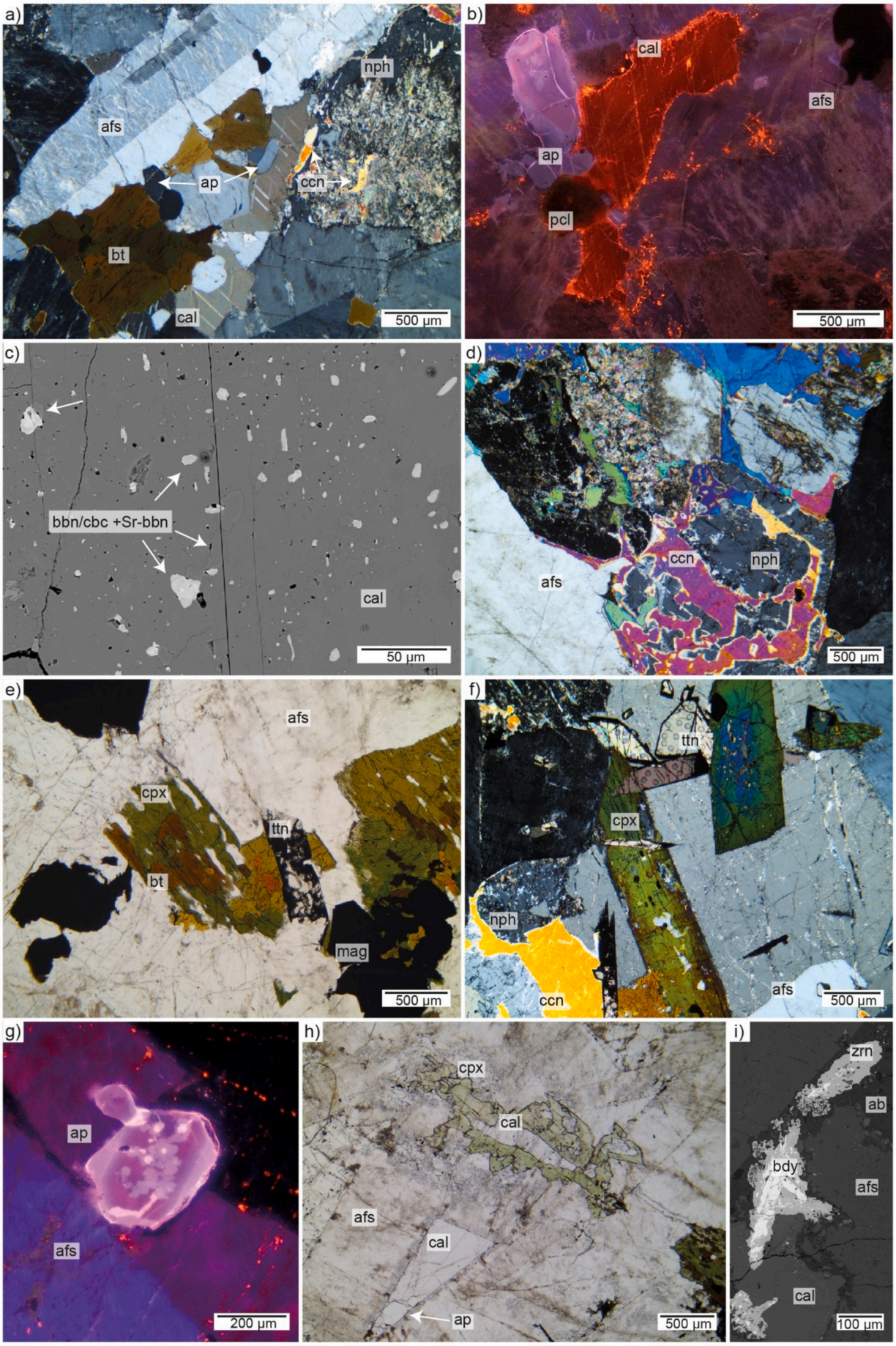

(caption on next page)

Fig. 2. Representative photomicrographs (plane polarized light and cathodoluminescence – CL) and backscattered electron (BSE) images of mineral assemblages of syenites (a – c) and nepheline syenites (d – i) from Ondurakorume. a) Large alkali feldspar crystals with biotite, nepheline altered to sericite and less to cancrinite, and interstitial calcite and apatite. b) CL image of alkali feldspar, interstitial calcite, pyrochlore and zoned apatite. c) BSE image of (Sr) – burbankite or carbocernaite inclusions in the interstitial calcite. d) Cancrinite and minor sericite replacing nepheline next to alkali feldspar. e) Biotite replacing clinopyroxene in association with titanite, magnetite, and alkali feldspar. f) Euhedral clinopyroxene showing zonation visible in the change of interference color next to titanite with laser ablation spots and nepheline altering to cancrinite. g) CL image of complexly zoned apatite in alkali feldspar. h) Interstitial assemblage of calcite, clinopyroxene and apatite between alkali feldspar. i) Baddeleyite-zircon replacement texture. Mineral abbreviations: afs – alkali feldspar, ap – apatite, nph – nepheline, ccn – cancrinite, bt – biotite, cal – calcite, pcl – pyrochlore, bbn – burbankite, cbc – carbocernaite, Sr-bbn – strontioburbankite, cpx – clinopyroxene, ttn – titanite, mag – magnetite, bdy – baddeleyite, zrn – zircon, ab – albite.

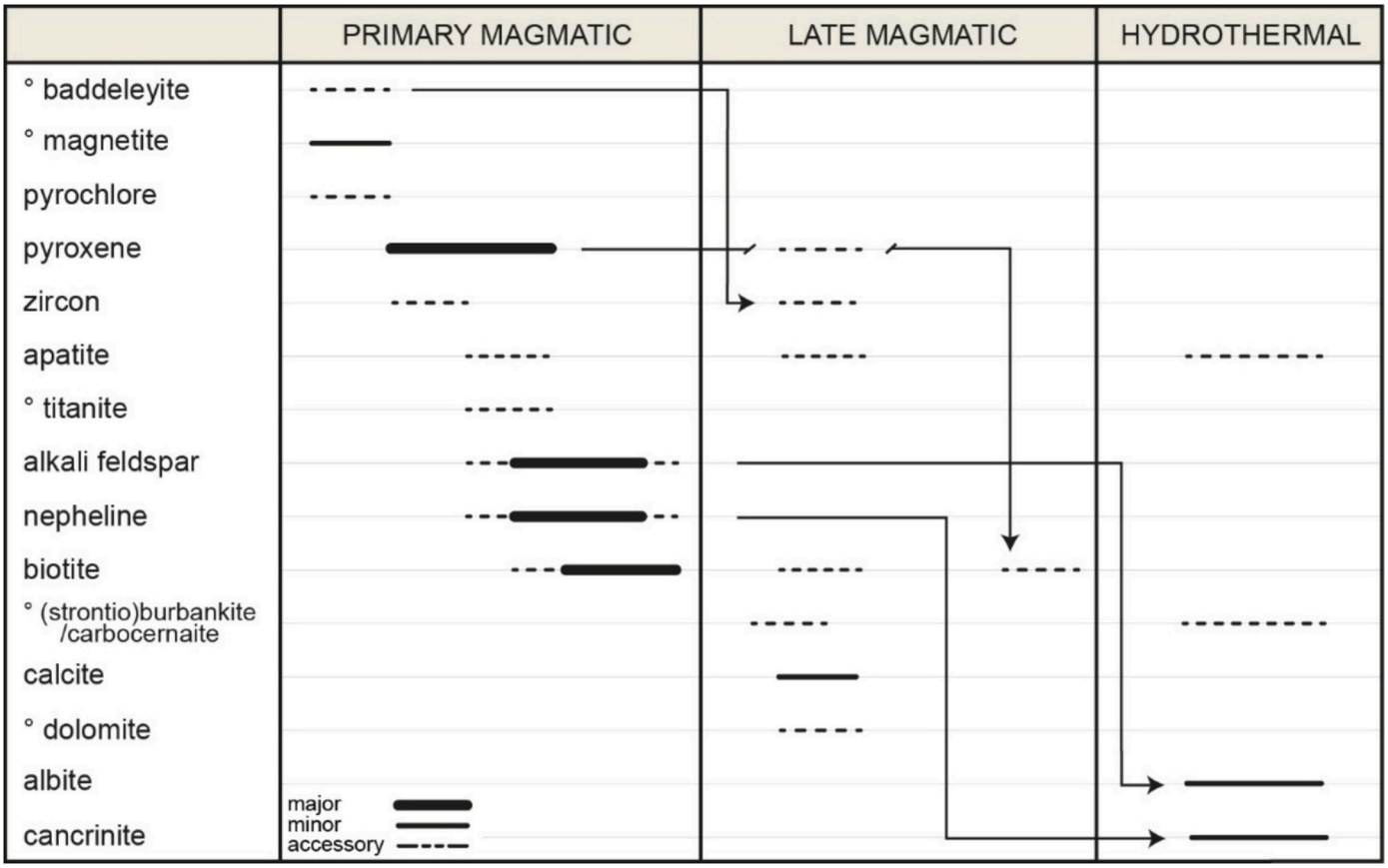

Fig. 3. Paragenetic scheme of syenites and nepheline syenites from Ondurakorume. Bold line – major phases, normal line – minor phases, dotted line – accessory phases. The "°" represents minerals that are only found in nepheline syenites, while arrows represent replacement relationships.

and abundant nepheline. Alkali feldspar (up to 1 cm) is twinned and perthitically exsolved, and nepheline (up to 0.5 cm) is partially altered to zeolites and sericite similarly to syenites, but shows large-scale replacement by cancrinite (Fig. 2d). In contrast to syenites, early magmatic subhedral to anhedral magnetite (up to 1 mm), euhedral titanite (0.8 mm) and euhedral to subhedral sodic clinopyroxene (2 mm) are common (Fig. 2e). Magnetite typically shows exsolution lamellae of ilmenite, which also occurs as a replacement of titanite on its rims or along cracks. Sodic clinopyroxene is partially replaced by biotite and sporadically calcite (Fig. 2e), and sometimes shows subtle zonation from green cores towards darker green rims, additionally seen in change of interference color (Fig. 2f). Apatite (0.3 mm) occurs as rounded subhedral, and as interstitial smaller grains with undulose extinction. Subhedral apatite shows similar CL colors as those found in syenites, with violet-blue cores, and light violet rims and patches in the core. Red zones are absent, but bright yellowish irregular rims are present (Fig. 2g). These apatite crystals are presumed to magmatic. Interstitial, anhedral apatite shows bright orange CL colors, and it is likely of hydrothermal origin. Carbonates (calcite, and sporadically dolomite, depending on the sample) are common accessory phases, mostly crystalizing interstitially between alkali feldspar (Fig. 2h). Other accessory phases are pyrochlore (0.3 mm), zircon (0.3 mm), and in sample (ON045) baddeleyite is partly replaced by zircon (Fig. 2i). A paragenetic scheme based on these textural observations is given for syenites and nepheline syenites on Fig. 3.

4.1.3. *Carbonatites*

Microscopy revealed more heterogeneity in the carbonatites than suggested by the schematic map (Fig. 1b) and they were therefore reclassified based on their mineralogy into dolomite-bearing (apatite) calcite carbonatites, apatite-bearing calcite carbonatites, and several types of carbonatitic dyke rocks, the majority being dolomite carbonatite dykes, and minority dolomite-bearing calcite carbonatite dykes.

Dolomite-bearing (apatite) calcite carbonatites (samples ON005, ON006A, ON006B, ON007) are calcite-dominated, but contain significant amounts of rhombohedral dolomite up to 2 mm in size (Fig. 4a). Starting from the rims, the dolomite is strongly altered to a very fine-grained opaque matrix composed of calcite, iron oxide ± dolomite (Fig. 4b). Coarse calcite displays two distinct shades of orange CL colors, with dark orange core and bright orange along the grain boundaries,

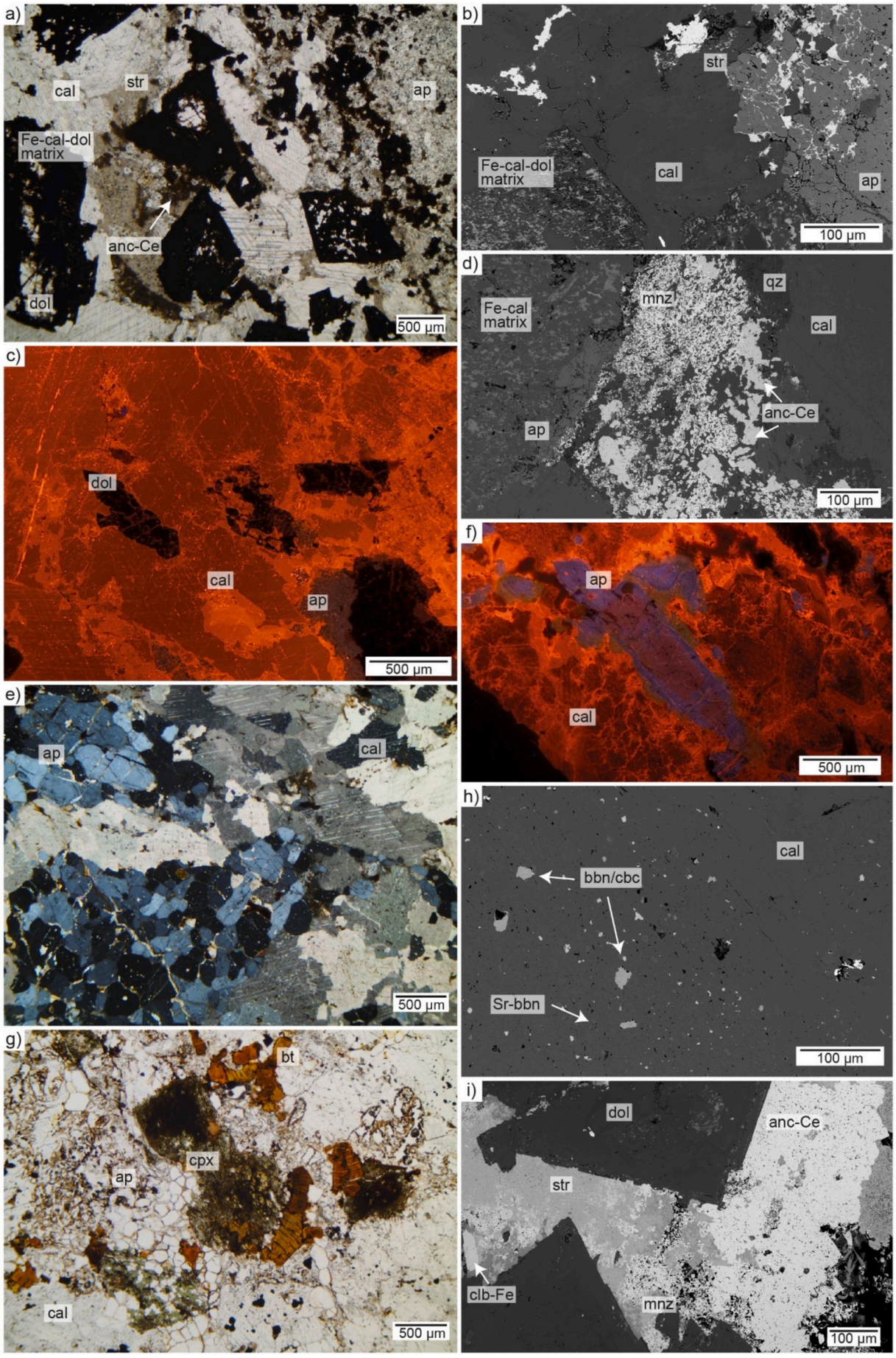

(caption on next page)

Fig. 4. Representative photomicrographs (plane polarized light and cathodoluminescence – CL) and backscattered electron (BSE) images of mineral assemblages of dolomite-bearing (apatite) calcite carbonatites (a – d), apatite-bearing calcite carbonatites (e – h), and dolomite carbonatites (i) from Ondurakorume. a) A dark iron-bearing carbonate matrix replacing euhedral dolomite next to interstitial strontianite and ancylite and an apatite band. b) BSE image of the Fe-bearing matrix, calcite, apatite and interstitial strontianite. c) CL image of fine-grained apatite and dolomite crystals (dark) in calcite with multiple generations (orange). d) BSE image of monazite and ancylite in association with quartz between calcite and apatite. e) Clustered apatites appear as schlieren in the calcite carbonatite. f) CL image showing three zones in an apatite crystal – red core, violet blue rim I, green rim II. g) Corroded clinopyroxene with biotite next to apatite and calcite. h) BSE image of burbankite or carbocernaite and strontioburbankite inclusions in calcite. i) BSE image of ancylite-strontianite replacement with columbite-(Fe) and monazite next to euhedral dolomite. Mineral abbreviations: cal – calcite, str – strontianite, dol – dolomite, anc-Ce – ancylite-(Ce), ap – apatite, mzn – monazite, qz – quartz, bbn – burbankite, cbc – carbocernaite, Sr-bbn – strontioburbankite, cpx – clinopyroxene, bt – biotite, clb-Fe – columbite-(Fe). For interpretation of the references to color, the reader is referred to the web version of this article.

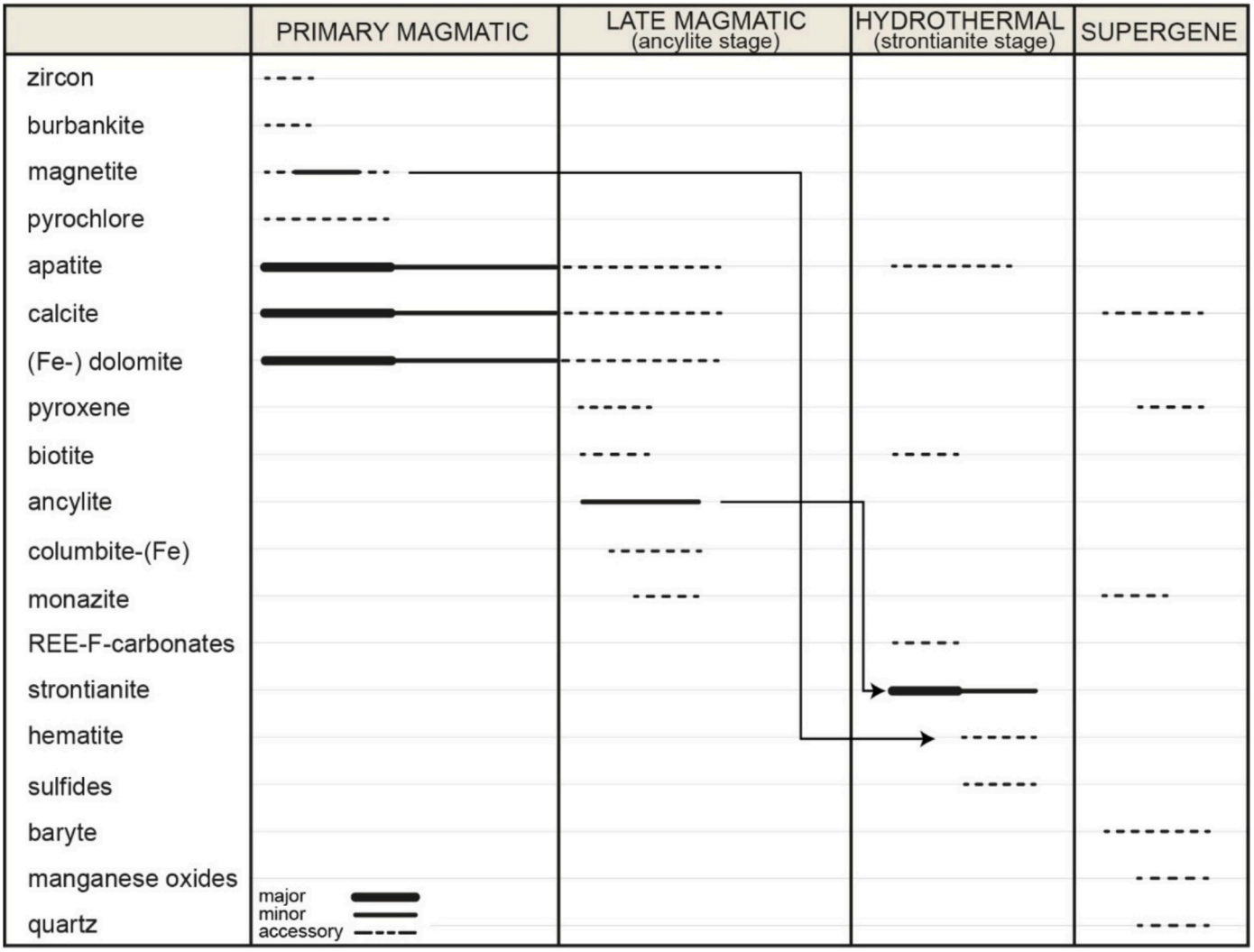

Fig. 5. Paragenetic scheme of carbonatites from Ondurakorume. Bold line – major phases, normal line – minor phases, dotted line – accessory phases. The arrows represent replacement relationships.

forming small patches near the rims, or following crystal defects and cracks (Fig. 4c). Abundant apatite (avg. 0.05 mm) forms fine-grained bands and patches in calcite (Fig. 4a), in which the crystals are usually cracked, almost brecciated, and cloudy with many cavities and pores. Cathodoluminescence of apatites showed a violet-blue CL color on larger grains and is otherwise darker when the crystals are fine-grained or the surfaces are highly porous (Fig. 4c). Apatite is absent in sample ON005. Strontianite is commonly associated with apatite and can occur on apatite grain boundaries (Fig. 4b) or along the rims of apatite bands. It can also be found in association with small sporadic patches of interstitial ancylite and small prismatic columbite-(Fe) (up to 0.05 mm), ± monazite, and ± quartz (Fig. 4d). Other accessory phases present are small euhedral pyrochlore, small amounts of baryte found in cavities, as well as small, likely supergene stage, monazite needles.

Apatite-bearing calcite carbonatites (samples ON021, ON036, ON038) contain up to 10 vol% of coarse apatite (0.4–1 mm), mostly occurring as schlieren (Fig. 4e). The grains are mostly subhedral and rounded, and occasionally contain up to 20 μm large inclusions of burbankite or carbocernaite in their core. Cathodoluminescence microscopy revealed red cores, followed by a violet-blue zone, occasionally succeeded by a green zone (Fig. 4f), that shows a spongy texture. Small amounts of subhedral magnetite with ilmenite exsolutions are present, as well as subhedral pyrochlore (0.2 mm), zircon (0.1 mm), and small needles of ilmenite. Clinopyroxene (up to 1 mm) is typically anhedral and often disintegrated with heavily corroded cores (Fig. 4g). Modest amounts of biotite form smaller crystals (around 0.15 mm in size) that

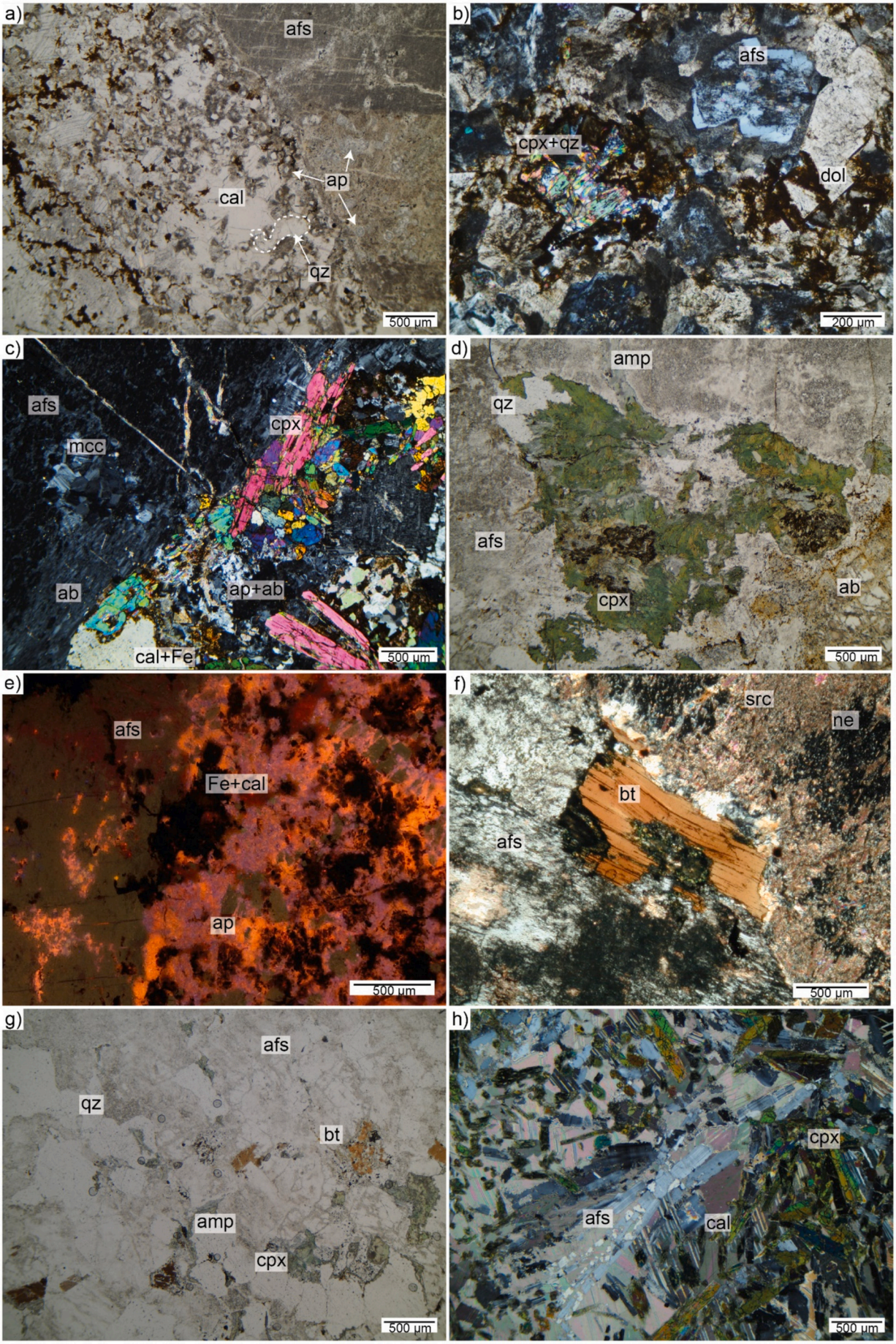

(caption on next page)

Fig. 6. Representative photomicrographs (plane polarized light and cathodoluminescence) images of mineral assemblages of carbonatite dykes (a – b), fenitized syenites (c – f), fenitized granite (g), and silicocarbonatite (h). a) Apatite crystals at the contact of carbonatite dyke and fenitized syenite with sporadic interstitial quartz. b) Clinopyroxene-quartz and alkali feldspar pockets in dolomite from a carbonatite dyke. c) Carbonate-apatite-albite pocket next to clinopyroxene, albite-rimmed alkali feldspar and fine-grained microcline. d) Fibrous clinopyroxene partially replacing quartz occurring with bluish amphibole next to altered alkali feldspars. e) CL image of turbid apatite next to a large alkali feldspar crystal. f) Remnants of nepheline replaced by sericite next to altered biotite and alkali feldspar. g) Biotite with clinopyroxene and sodic amphibole crystalizing at quartz grain boundaries. h) Alkali feldspar in calcite with clinopyroxene. Mineral abbreviations: afs – alkali feldspar, ap – apatite, cal – calcite, qtz – quartz, cpx – clinopyroxene, dol – dolomite, ab – albite, mcc – microcline, amp – amphibole, bt – biotite, src – sericite, ne – nepheline.

are slightly banded (Fig. 4g), and occasionally have iron oxide along cleavage cracks. Coarse calcite is mostly anhedral and often contains rounded or vermicular inclusions of burbankite or carbocernaite (a few tens of μm in size, Fig. 4h). Other REE-bearing phases, such as monazite, ancylite, and synchysite-(Ce), are present in small amounts and mostly occur in cavities. Baryte, pyrite, and occasionally sphalerite can be found, as well as hematite as a magnetite replacement. Additionally, secondary calcite veining is observed.

Dolomite carbonatite dykes (samples ON017, ON022A, ON028) are rich in subhedral, sometimes Fe-bearing, dolomite and can contain up to 30 vol% of calcite. Sample ON028 additionally contains fibrous, bluish to greenish amphibole. Notable are abundant interstitial assemblages (up to 15 vol%) consisting of subhedral to anhedral ancylite (0.4 mm), prismatic columbite-(Fe) (0.1 mm) and prismatic monazite (<0.1 mm) (Fig. 4i). Ancylite and monazite are partially replaced by large amounts of strontianite, presumably at hydrothermal conditions. Hematite/goethite and small amounts of baryte are generally present. Quartz occurs either as late-stage veinlets, or as an interstitial phase together with ancylite, monazite, columbite-(Fe), and strontianite. Late calcite veins cut through the whole sample, and it is assumed they represent a later, probably hydrothermal alteration of dolomite carbonatite. A paragenetic scheme for carbonatites based on textures is shown on Fig. 5.

In calcite carbonatite dykes (samples ON010A, ON019, ON030, ON031), dolomite can account for up to 30 vol%. Apatite is a major phase, forming layers of anhedral and fine-grained cloudy grains, with one of the samples (ON031) displaying apatite with a rectangular shape (Fig. 6a) at the contact to a fenite, where the core is rounded and homogeneous, and the rims are spongy and turbid. The CL color of the core is violet blue, while the rims have a light orange color. Additional phases are interstitial strontianite (usually in association with ancylite), monazite needles, and in some cases quartz. In one sample (ON030), clinopyroxene (up to 0.2 mm) is associated with euhedral to subhedral alkali feldspar ± quartz, forming pockets in the carbonatite (Fig. 6b). Alkali feldspar is often rounded and partly altered to clay minerals. Small amounts of baryte, brookite, pyrochlore, Mn oxides, and REE-bearing phases like burbankite or carbocernaite, and occasionally britholite are present.

4.1.4. *Fenitized rocks and silicocarbonatite*

Fenitized (nepheline) syenites (samples ON010B, ON023, ON033) largely consist of centimeter-sized perthitically exsolved alkali feldspar, occasionally with albite rims (Fig. 6c). In one sample (ON023), alkali feldspar is partially replaced by fine-grained microcline (Fig. 6c). Abundant green sodic clinopyroxene is euhedral to subhedral, showing variable grain-sizes and textures, ranging from very fine-grained vein fillings and fibrous aggregates to textures with elongated, up to 1.5 mm sized crystals. In one sample (ON033) clinopyroxene is observed to replace quartz (Fig. 6d). Pale blue sodic amphibole is occasionally present as smaller fibrous aggregates or is intergrown with clinopyroxene (Fig. 6d). Calcite commonly occurs as veins and patches in alkali

Table 3
Representative EPMA measurements of clinopyroxenes from different lithologies present on Ondurakorume. Fe^{3+} was estimated using the equation proposed by Droop (1987). Concentrations of K and Cr were measured as well, but were below the detection limit in all measurements.

SAMPLE	045	046	046	047	038	031	023	033	029	027
LITHOLOGY	nepheline syenite	nepheline syenite	nepheline syenite	nepheline syenite	apatite-b. calcite carbonatite	carbonatite dyke	fenitized syenite	fenitized syenite	fenitized granite	silicocarbonatite
MINERAL	diopside	hedenbergite	aegirine	aegirine-augite	aegirine-augite	aegirine	aegirine	aegirine-augite	aegirine	aegirine- augite
SiO_2	50.11	49.61	52.31	50.47	52.64	52.30	52.43	51.60	52.67	52.67
TiO_2	0.57	0.40	0.16	0.50	0.47	2.15	2.08	1.17	7.56	0.75
ZrO_2	0.22	0.48	b.d.l.	1.56	0.48	0.16	0.22	0.13	b.d.l.	0.13
Al_2O_3	1.52	1.21	1.38	1.05	0.66	0.29	0.41	0.26	0.14	0.64
FeO	10.28	12.44	4.83	8.60	6.18	3.89	1.48	3.97	3.89	5.95
Fe_2O_3	8.02	11.19	27.79	19.07	16 23	26.31	27.54	23.37	18.93	15.44
MnO	0.67	0.91	b.d.l.	0.72	0.27	b.d.l.	b.d.l.	0.33	0.27	0.57
MgO	7.11	3.45	0.17	1.21	5.34	0.82	1.66	2.46	2.22	5.45
CaO	18.98	14.84	0.37	7.33	9.91	0.70	1.12	5.68	0.19	11.44
Na_2O	2.72	4.62	12.30	8.80	7.54	12.57	12.67	10.10	13.23	7.08
TOTAL	100.21	99.18	99.40	99.32	99.72	99.23	99.70	99.10	99.13	100.12
formulae based on 4 cations and 6 oxygens										
Si^{4+}	1.93	1.96	2.02	1.98	2.01	2.02	2.00	2.00	2.00	2.00
Ti^{4+}	0.02	0.01	<0.01	0.01	0.01	0.06	0.06	0.03	0.22	0.02
Zr^{4+}	<0.01	0.01	<0.01	0.03	0.01	<0.01	<0.01	<0.01	<0.01	<0.01
Al^{3+}	0.07	0.06	0.06	0.05	0.03	0.01	0.02	0.01	0.01	0.03
Fe^{2+}	0.33	0.41	0.16	0.28	0.20	0.13	0.05	0.13	0.12	0.19
Fe^{3+}	0.23	0.33	0.81	0.56	0.47	0.76	0.79	0.68	0.54	0.44
Mn^{2+}	0.02	0.03	<0.01	0.02	0.01	<0.01	<0.01	0.01	0.01	0.02
Mg^{2+}	0.41	0.20	0.01	0.07	0.30	0.05	0.09	0.14	0.13	0.31
Ca^{2+}	0.78	0.63	0.02	0.31	0.41	0.03	0.05	0.24	0.01	0.47
Na^{+}	0.20	0.35	0.92	0.67	0.56	0.94	0.94	0.76	0.97	0.52

Note. b. – bearing, b.d.l. – below detection limit.

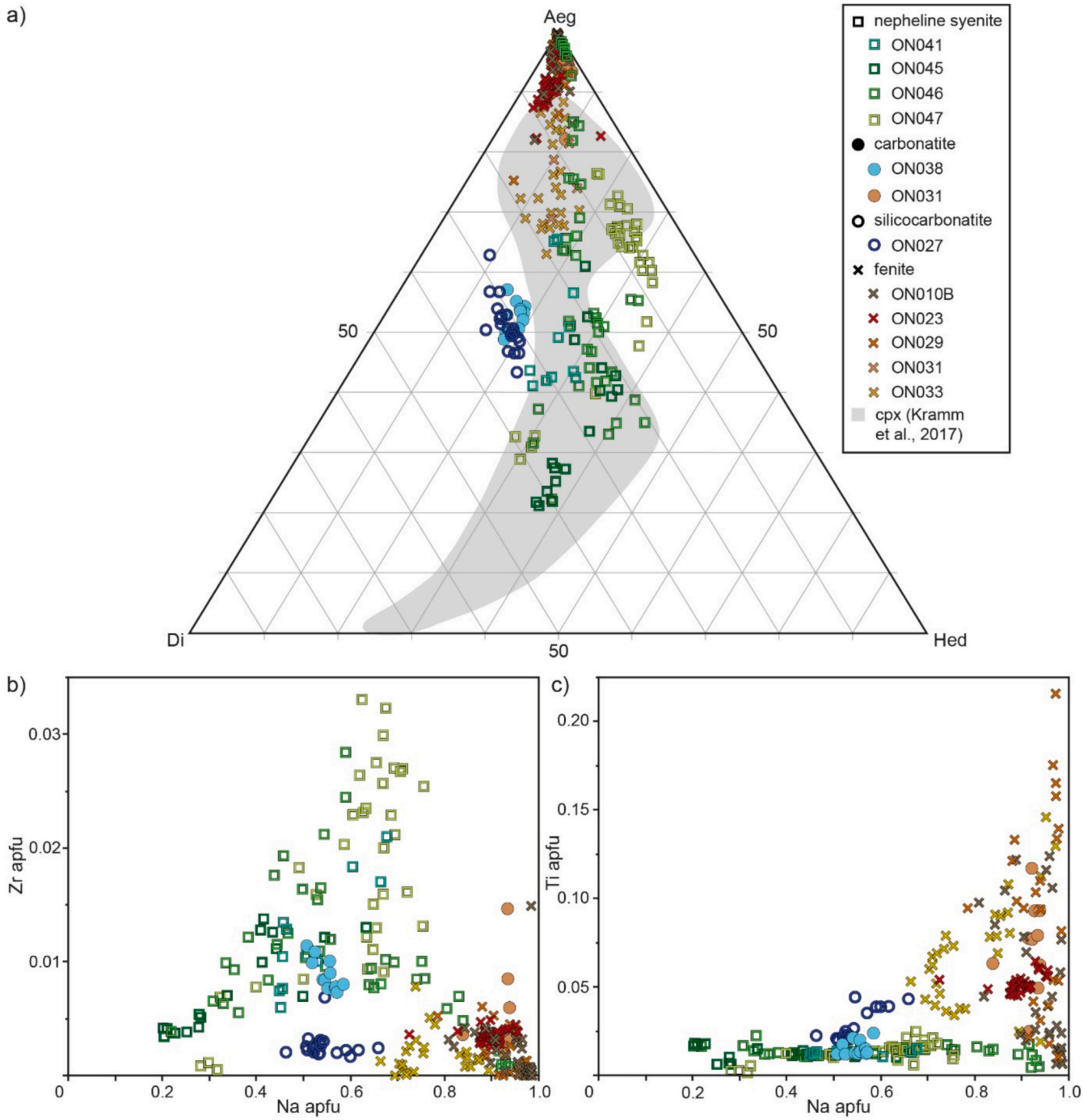

Fig. 7. Chemical variations of clinopyroxene in rocks from Ondurakorume. a) Ternary diagram with diopside-hedenbergite-aegirine components representing rocks from Ondurakorume which generally overlap with a grey field encompassing clinopyroxenes from nepheline syenites and tinguaites from spatially associated Kalkfeld complex (Kramm et al., 2017). b) Binary plot showing Na content vs Zr (apfu), with an increase of Zr in nepheline syenites and a slight increase in carbonatites. c) Binary plot showing Na content vs Ti (apfu), with an increase of Ti in fenites and one carbonatite sample (in contact with a fenite).

feldspar, and it is usually in association with apatite and albite (Fig. 6c). Apatite is generally spongy and turbid, anhedral and up to 0.2 mm in size. It has a bright orange cathodoluminescence color, often seen as transitioning from commonly present violet blue color (Fig. 6e). Remnants of nepheline can be found sporadically, although it is mostly altered to sericite and partially cancrinite (Fig. 6f). Common accessory phases include brookite, baryte, pyrochlore, iron oxides, and less so mica, sphalerite and zircon.

Fenitized granite (sample ON029) is fine-grained and contains rounded quartz (< 1 mm), perthitically exsolved alkali feldspar (up to 1.5 mm), and plagioclase (up to 1 mm) that is typically altered to clay minerals. Green sodic clinopyroxene and small amounts of blue sodic amphibole form mostly fibrous aggregates and veins along grain boundaries (Fig. 6g). Precursor biotite is commonly altered to fine-grained clinopyroxene, ilmenite, and iron oxides. Zircon, monazite and iron oxides are common accessory phases, while apatite (with a yellow CL color), baryte, and calcite are rare.

Silicocarbonatite (ON027) contains calcite, microcline and sodic clinopyroxene, each occupying about 30 vol%. Rounded and elongated microcline crystals (up to 1.8 mm) are replaced by small amounts of

Table 4
Representative EPMA measurements of apatites from different lithologies present on Ondurakorume. Additionally, Mn, Mg, La, Pr, U, S and Cl were measured, but are very close to or below the detection limit in <95 % of the samples, and were therefore omitted from the table.

SAMPLE	041	037	006A	021	038	031	010B	023	029	027
LITHOLOGY	nepheline syenite	syenite	dolomite-b. apatite calcite carbonatite	apatite-b. calcite carbonatite	apatite-b. calcite carbonatite	carbonatite dyke	fenitized syenite	fenitized syenite	fenitized granite	silicocarbonatite
SiO_2	0.11	0.14	b.d.l.	0.13	b.d.l.	b.d.l.	b.d.l.	b.d.l.	b.d.l.	0.27
FeO	b.d.l.	b.d.l.	b.d.l.	b.d.l.	0.09	b.d.l.	b.d.l.	0.12	0.08	0.36
CaO	54.96	54.94	54.49	54.49	53.66	53.87	54.40	54.27	53.02	54.38
SrO	0.90	1.05	1.50	1.27	1.36	0.57	0.70	1.08	1.10	1.08
Na_2O	0.17	0.18	0.11	0.11	0.40	0.46	0.26	0.36	0.50	0.15
K_2O	b.d.l.	b.d.l.	b.d.l.	b.d.l.	b.d.l.	0.06	b.d.l.	b.d.l.	b.d.l.	0.13
Ce_2O_3	0.28	0.39	0.34	0.42	0.58	b.d.l.	b.d.l.	b.d.l.	0.52	b.d.l.
Nd_2O_3	b.d.l.	b.d.l.	b.d.l.	b.d.l.	0.22	0.22	b.d.l.	b.d.l.	0.27	b.d.l.
P_2O_5	41.92	41.81	42.14	41.74	41.08	41.01	41.93	41.36	41.24	41.68
F	2.90	2.37	3.00	2.34	1.91	2.59	2.34	3.07	3.21	2.58
H_2O	0.41	0.66	0.36	0.67	0.85	0.52	0.66	0.31	0.23	0.56
Total	102.11	101.89	102.33	101.56	100.63	99.71	100.78	101.22	100.59	101.85
O=F, Cl	100.89	100.89	101.07	100.57	99.82	98.62	99.79	99.93	99.23	100.76
formulae based on 13 total anions, with $\sum$ (OH, F, Cl) = 1										
Si^{4+}	0.01	0.01	<0.01	0.01	<0.01	<0.01	<0.01	<0.01	<0.01	0.02
Fe^{2+}	<0.01	<0.01	<0.01	<0.01	0.01	<0.01	<0.01	0.01	0.01	0.03
Ca^{2+}	4.94	4.94	4.90	4.92	4.91	4.95	4.92	4.94	4.86	4.90
Sr^{2+}	0.04	0.05	0.07	0.06	0.07	0.03	0.03	0.05	0.05	0.05
Na^{+}	0.03	0.03	0.02	0.02	0.07	0.08	0.04	0.06	0.08	0.02
K^{+}	<0.01	<0.01	<0.01	<0.01	<0.01	0.01	<0.01	<0.01	<0.01	0.01
Ce^{3+}	0.01	0.01	0.01	0.01	0.02	<0.01	<0.01	<0.01	0.02	<0.01
Nd^{3+}	<0.01	<0.01	<0.01	<0.01	0.01	0.01	<0.01	<0.01	0.01	<0.01
P^{5+}	2.98	2.97	2.99	2.98	2.97	2.98	3.00	2.97	2.99	2.97
F^{-}	0.77	0.63	0.80	0.62	0.52	0.70	0.63	0.82	0.87	0.69
OH^{-}	0.23	0.37	0.20	0.38	0.48	0.30	0.37	0.17	0.13	0.31

Note. b. – bearing, b.d.l. – below detection limit.

albite, and both are getting corroded by surrounding calcite (Fig. 6h). Cathodoluminescence of calcite showed three distinct orange colors, ranging from dark to bright orange, revealing different calcite generations. Calcite occasionally has rounded burbankite or carbocernaite inclusions, a few tens of μm in size. Clinopyroxene (up to 1.5 mm in size) forms euhedral to subhedral partially corroded prismatic crystals with many cracks, that occasionally form aggregates. Small, but euhedral pyrochlore is a common accessory phase, along with baryte and iron oxides. Zircon and apatite are rare, and ancylite and monazite can be found in cavities.

4.2. Mineral compositions

4.2.1. Clinopyroxene

Clinopyroxene formulae are based on 6 oxygens and 4 cations, and representative analyses are shown in Table 3. Clinopyroxenes from nepheline syenites show the highest variability of all lithologies. Most of them are aegirine-augites, with compositions of $Di_{40\text{-}5}Hed_{36\text{-}15}Aeg_{21\text{-}65}$ (Fig. 7a), while some of the grains are aegirines, with up to 83 mol% of aegirine component. They can also contain up to 1.7 wt% of ZrO_2 (0.033 apfu Zr; Fig. 7b). Clinopyroxenes in fenites are mostly aegirine (up to 95 mol% Aeg), with negligible Di and Hed components (Fig. 7a) and average Ti-Aeg component of about 10 mol% (maximum 43 mol% Ti-Aeg, which attributes to 7.5 wt% TiO_2 (0.22 apfu Ti; Fig. 7c). Clinopyroxene from a carbonatite (sample ON038) is aegirine-augite ($Di_{30\text{-}24}Hed_{17\text{-}13}Aeg_{53\text{-}44}$), and silicocarbonatite sample (ON027) contains aegirine-augite with a similar composition ($Di_{32\text{-}24}Hed_{22\text{-}8}Aeg_{55\text{-}41}$).

4.2.2. Apatite

Apatite formulae are based on 13 total anions and representative analyses are shown in Table 4. The amount of OH was calculated assuming charge balance and fully occupied Z position (Σ (F, OH, Cl) = 1), the potential incorporation of CO_3 was not considered in these calculations. Overall, apatites have very low Cl (<0.006 apfu) and S (<0.005 apfu) contents, and are mostly fluorapatites, except for some hydroxylapatites in carbonatites, with up to 0.73 apfu (73 mol%) calculated OH (Fig. 8a). In general, Sr contents range between 0.5 and 1.5 wt% (0.03–0.07 apfu), with apatite from one dolomite carbonatite (ON028) having up to 7 wt% SrO (0.37 apfu; Fig. 8b). Sodium shows slightly higher contents in apatites with orange CL color, where it can reach up to 1.1 wt% (0.19 apfu), although it is mostly under 0.5 wt% (0.08 apfu; Fig. 8c). Both Sr and Na variability does not seem to depend on lithology, but rather on later e.g. hydrothermal events. In carbonatites, REE (La + Ce + Pr + Nd) are typically below the detection limit, although where measurable, they can reach up to 1.4 wt% (0.05 apfu). They show somewhat higher values in nepheline syenites, up to 2.5 wt% (0.07 apfu). Similarly, Si contents in carbonatites are low, reaching a maximum of 0.23 wt% (0.02 apfu; Fig. 8d), while in nepheline syenites it reaches up to 0.5 wt% (0.04 apfu; Fig. 8d). Other trace elements are generally low, with Fe and Mn being above the detection limit only in carbonatites, with maximum values of 0.57 and 0.36 wt% (0.04 and 0.03 apfu), respectively.

4.2.3. Mica

Mica formulae are based on eight cations (with only Si, Al and Fe^{3+} on tetrahedral position) and 12 oxygens, with OH and O calculated assuming Σ (OH, F, Cl, O) = 2. Based on these assumptions, Fe^{3+} only had a very minor role in substituting for Al, with a maximum value of 0.09 apfu. Representative analyses are shown in Table 5. Mica from all samples (except for sample ON033, which is shortly described separately below), belongs to the biotite series with X_{Mg} values between 0.65 and 0.18 (Fig. 9). The highest X_{Mg} values are exhibited by mica from apatite-bearing calcite carbonatite (ON038, avg. X_{Mg} = 0.45) and fenitized granite (ON029, X_{Mg} = 0.40–0.65), and the lowest from nepheline syenite (X_{Mg} = 0.18–0.37). The contents of Ti range from 3.5 to 5.2 wt% TiO_2 (0.21–0.32 apfu) in nepheline syenites, syenites and fenites, but is lower in carbonatites, where it reaches maximum of about 3 wt% TiO_2 (0.18 apfu). The contents of Mn are typically below 0.5 wt% MnO, but

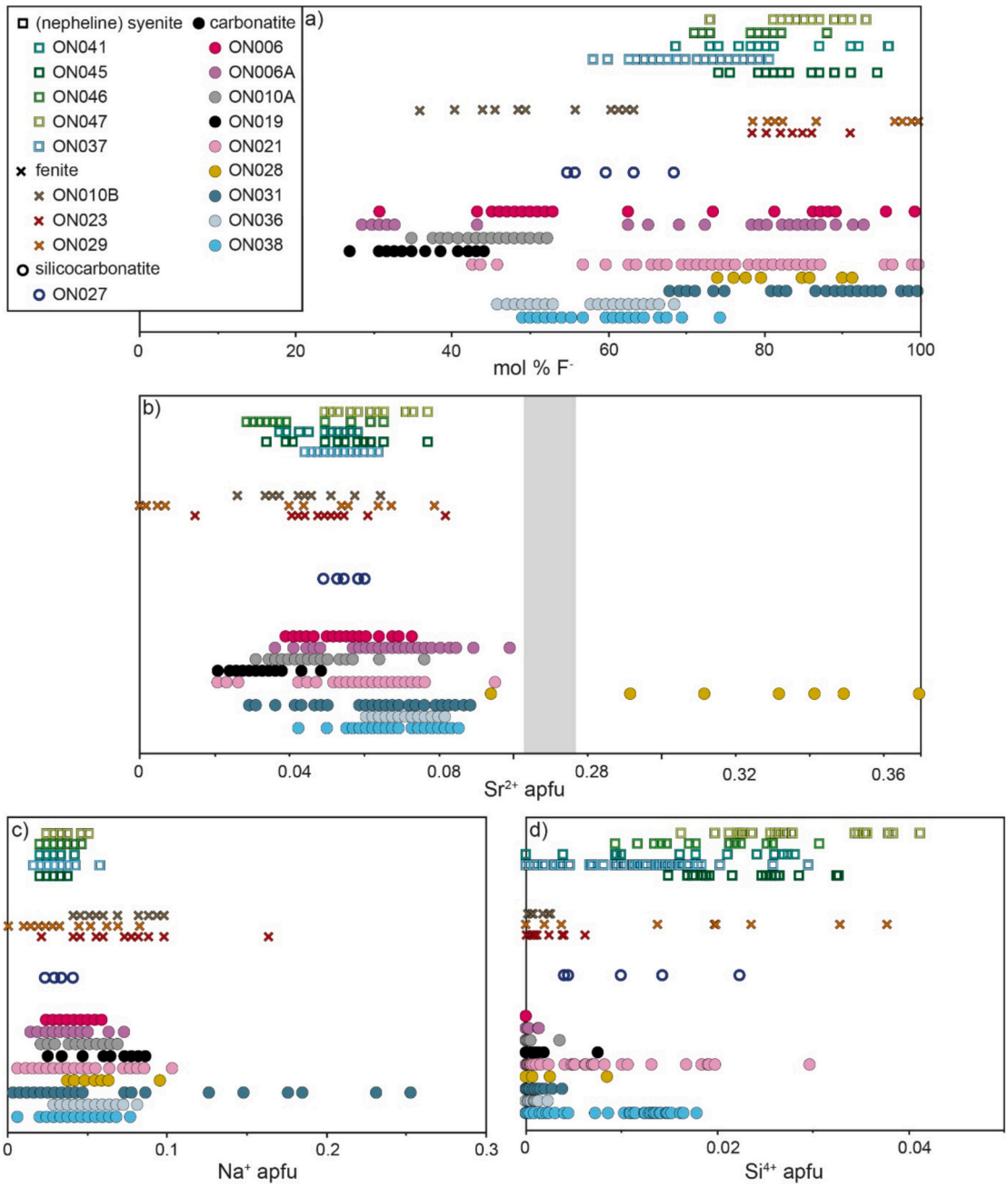

Fig. 8. Chemical variations of apatite in, from top to bottom, nepheline syenites, fenites, silicocarbonatite, and carbonatites. a) Compositional range of F and OH (mol. %), since Cl is under the detection limit. b) Range of Sr content (apfu), where a grey block represents a large gap from roughly 0.1 to 0.29 apfu. c) and d) show compositional ranges of Na and Si (apfu) in apatites, respectively.

may reach 1.7 wt% MnO (0.12 apfu) in nepheline syenites. The dominant cation on interlayer position is K, with almost negligible substitutions with Na, Ca, and Ba, which together account for around 0.03 apfu. Contents of F reach 1.5 wt% (0.38 apfu), while Cl is below the detection limit. Sample ON033 (fenitized (nepheline) syenite) is notable for its completely different mica, with high Si content (up to 59 wt%), which attributes to an excess of Si on tetrahedral position of up to 0.13 apfu. It is almost the Mg end-member with up to 21 wt% ($X_{Mg} = 0.99$), and very rich in K (up to 11.5 wt%) and F (up to 9.2 wt%), and very poor in Ti, Fe, Al, and Na. With totals of around 97 wt% (after F-correction and including calculated water), and the excess of Si, the presence of Li is indicated. This was confirmed by laser ablation, which resulted in 14,500–16,500 ppm Li (Supplementary File 4), which, with the EPMA analyses gives a composition close to the ideal formula of tainiolite (also spelled taeniolite; $KLiMg_2[Si_4O_{10}]F_2$). Tainiolite was reported before from fenites from Dicker Willem, Namibia (Cooper et al., 1995) and from Haast River, New Zealand (Cooper et al., 2016).

4.2.4. *Amphibole*

For two amphibole-bearing samples, formulae calculations were done using the Excel spreadsheet of Locock (2014). Amphibole from fenitized syenite (ON033) is magnesio-arfvedsonite (Mg# = 0.58–0.70) and contains 1.65–3 wt% F (0.77–1.36 apfu), with Cl contents below the detection limit in all measurements. Given that the recalculated Si content exceeded 8 apfu (like in mica from this sample, see above), and the C position was up to 0.2 apfu lower than the ideal of 5, it is suggested that this amphibole may be Li-bearing. Addition of 0.05–0.4 wt% of Li_2O to the analyses resolves both the Si surplus and the C position deficiency.

Table 5
Representative EPMA measurements of micas from different lithologies present on Ondurakorume. Contents of Zr, Ca, Ba and Cl were in majority of the samples below the detection limit and were omitted from the table.

SAMPLE	039	038	041	046	037	047	029	033
LITHOLOGY	syenite	apatite-b. calcite carbonatite	nepheline syenite	nepheline syenite	syenite	nepheline syenite	fenitized granite	fenitized syenite
MINERAL	annite	annite	annite	annite	annite	annite	annite	tainiolite
SiO_2	35.71	36.70	35.52	35.24	35.89	34.66	37.60	58.98
TiO_2	4.67	2.94	4.69	4.68	4.42	3.71	3.50	0.03
Al_2O_3	12.08	12.03	11.61	10.96	11.48	11.09	11.48	0.31
Fe_2O_3	b.d.l.	b.d.l.	0.03	1.30	0.16	0.32	0.16	b.d.l.
FeO	26.05	21.68	26.76	26.57	24.57	29.84	19.07	0.27
MnO	0.25	0.17	0.16	0.57	0.24	1.69	0.23	0.02
MgO	7.66	11.57	7.33	7.10	8.79	4.68	12.99	20.52
Na_2O	0.22	0.32	0.27	0.22	0.25	0.16	0.11	0.24
K_2O	9.63	8.86	9.20	9.33	9.27	9.02	9.98	11.47
F	1.24	0.90	1.27	0.39	0.39	0.43	2.70	9.20
H_2O	2.36	2.66	2.23	2.69	2.71	2.73	1.89	0.00
Total	99.94	97.99	99.08	99.06	98.26	98.32	97.94	101.04
O=F, Cl	99.42	97.61	98.54	98.89	98.10	98.14	96.79	97.16
formulae based on 8 cations, 12 oxygen, and $\sum$ (OH, F, Cl, O) = 2								
Si^{4+}	2.87	2.92	2.89	2.87	2.90	2.89	2.94	4.13
Ti^{4+}	0.28	0.18	0.29	0.29	0.27	0.23	0.21	<0.01
Al^{3+}	1.14	1.13	1.11	1.05	1.09	1.09	1.06	0.03
Fe^{3+}	<0.01	<0.01	<0.01	0.08	0.01	0.02	0.01	<0.01
Fe^{2+}	1.75	1.44	1.82	1.81	1.66	2.08	1.25	0.02
Mn^{2+}	0.02	0.01	0.01	0.04	0.02	0.12	0.02	<0.01
Mg^{2+}	0.92	1.37	0.89	0.86	1.06	0.58	1.51	2.14
Na^{+}	0.03	0.05	0.04	0.03	0.04	0.03	0.02	0.03
K^{+}	0.99	0.90	0.95	0.97	0.95	0.96	0.99	1.02
F^{-}	0.31	0.23	0.33	0.10	0.10	0.11	0.67	2.04
OH^{-}	1.26	1.41	1.21	1.46	1.46	1.52	0.98	0.00

Note. b – bearing, b.d.l. – below detection limit.

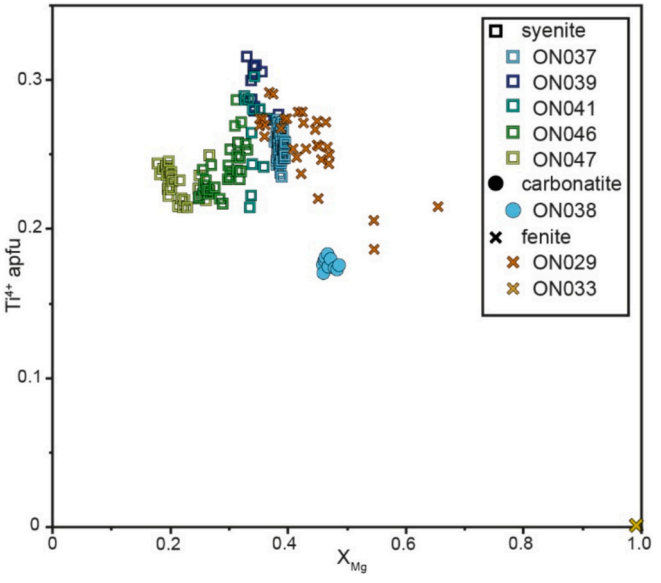

Fig. 9. Binary diagram showing X_{Mg} vs Ti (apfu) in biotites from syenites, nepheline syenites, carbonatites, and fenites from Ondurakorume.

The same issue has been previously raised e.g. for amphibole in fenites from the Alnö carbonatite complex (Sweden), although an analytical error or errors in the formula calculation have been assumed (Morogan and Woolley, 1988). These amphiboles and similar ones in fenites from the Fen complex (Norway) were later assumed to be Li-bearing (Martin, 2007) and because of a lack of laser ablation data, we consider the presence of Li (as in mica from the same sample, see above) as a likely solution. Amphibole from amphibole-bearing dolomite carbonatite (ON028) is magnesio-riebeckite (Mg# = 0.40–0.47), with low Ca (0.025–0.28 apfu) and K (up to 0.24 apfu). They are poor in F (up to 0.31 wt%), and Cl is below the detection limit. Measurements for these two samples can be found in Supplementary File 2.

4.3. U-Pb age dating

Obtained U-Pb ages on zircon, titanite and apatite from Ondurakorume, Kalkfeld, Etaneno, and Osongombo are given in Table 6 and illustrated in Fig. 10a-h (all obtained U-Pb data are given in Supplementary File 3). For Etaneno, the obtained zircon and titanite ages (mean of 139.2 ± 6.7 Ma), are similar to previous data (Müller, 1996; Sun et al., 2024), while the apatite ages are slightly younger (mean of 122.8 ± 3.8 Ma). Two nepheline syenites from Kalkfeld returned Early Triassic ages for titanite (249.6 ± 3.2 and 249.4 ± 2.9 Ma) that are similar to recent age data (Rb—Sr isochron from mineral separates, 242 ± 6.5 Ma) from Kramm et al. (2017). Again, the obtained apatite ages show a somewhat younger result with a large error (217.4 ± 24.5 Ma). Nepheline syenites from Ondurakorume yield Permian ages for titanite (272.1 ± 1.5 Ma), confirming recent age data obtained on zircons from a syenite (275.3 ± 7.9 Ma; Sun et al., 2024). Apatite from the same samples resulted in a younger age (257.5 ± 4.6 Ma), and carbonatite samples yielded an even younger age (248.1 ± 4.8 Ma).

Because of their limited size, apatites from Osongombo carbonatite dykes could not be dated by the applied method. Apatite from the surrounding marbles (in one case from the contact with the carbonatite dyke (OS006), in the other case ~50 m away (OS019)) yield Ordovician ages of 479.6 ± 2.6 and 465.1 ± 7.0 Ma, respectively.

Table 6
U-Pb ages of the Kalkfeld group complexes.

Sample	Locality	Lithology	Mineral	Age (Ma)	± 2σ	n	MSWD
ON021	Ondurakorume	apatite-b. calcite carbonatite	ap	248.1	4.8	63	1.44
ON041	Ondurakorume	nepheline syenite	ap	257.5	4.6	10	0.90
ON046	Ondurakorume	nepheline syenite	ttn	271.7	1.5	29	1.10
KF037	Kalkfeld	nepheline syenite	ttn	249.6	3.2	33	1.62
KF048	Kalkfeld	nepheline syenite	ap	217.4	24.5	11	1.27
KF048	Kalkfeld	nepheline syenite	ttn	249.4	2.9	50	1.38
ET001	Etaneno	nepheline syenite	ap	121.9	5.5	33	1.98
ET011	Etaneno	syenite	ap	120.5	1.3	32	1.96
ET011	Etaneno	syenite	zrn	143.46	0.67	13	5.0
ET019	Etaneno	nepheline syenite	ap	125.3	3.1	24	1.67
ET035	Etaneno	nepheline syenite	ap	123.6	5.2	22	1.83
ET035	Etaneno	nepheline syenite	ttn	135.3	18.5	28	0.72
ET035	Etaneno	nepheline syenite	zrn	138.81	0.87	28	2.9
OS006	Osongombo	marble-carbonatite contact	ap	479.6	2.6	21	1.19
OS019	Osongombo	marble	ap	465.1	7.0	30	14.43

Note. b. – bearing, ap – apatite, ttn – titanite, zrn – zircon, n – number of measurement points, MSWD – mean squared weighted deviation.

5. Discussion

5.1. Petrological and geochemical evolution of the Ondurakorume carbonatite complex

5.1.1. Magmatic evolution of syenites and carbonatites

Local syenite rafts and mega-xenoliths within the carbonatite bodies (in the north and east of the complex; Fig. 1b) demonstrate that syenites and nepheline syenites predate (at least partly) the emplacement of carbonatites. In nepheline syenites, early clinopyroxene is aegirine-augite evolving towards aegirine-rich compositions, similar as was observed for Kalkfeld (Fig. 7a; Kramm et al., 2017). Although accessory zircon is present in the nepheline syenites, a slight increase of Zr content in clinopyroxene with evolution is observed (Fig. 7b), which is a known feature in alkaline systems (e.g. Jones and Peckett, 1981; Mann et al., 2006; Andersen et al., 2012). The contents of Ti, however, remain low (Fig. 7c), possibly due to significant fractionation of Ti-bearing phases (e.g. magnetite, titanite).

Some of the nepheline syenites (ON046) contain interstitial calcite associated with aegirine-rich clinopyroxene (Fig. 7a), forming pockets between already crystallized large euhedral alkali feldspar and nepheline (Fig. 2h). This calcite contains primary burbankite or carbocernaite inclusions, which is also observed in the magmatic calcite and apatite from most carbonatites (e.g. Fig. 3h). Some of the pockets additionally contain biotite, and apatite with a slightly higher Si content compared to apatite from the carbonatites (Fig. 8e), and primary baddeleyite being replaced by zircon (Fig. 2i). These textures and mineral compositions are interpreted to result from localized infiltration of a relatively alkali-rich carbonatitic melt (based on the presence of burbankite or carbocernaite inclusions in the calcite) into the syenite crystal mush, causing interaction and element exchange (Chakhmouradian and Dahlgren, 2021).

Clinopyroxene compositions from a carbonatite (sample ON038) that was collected close to the nepheline syenite body, and from a silicocarbonatite (ON027) sampled close to the granitic country rocks are not falling on the evolutionary trend recorded in the nepheline syenites (Fig. 7a). Thus, clinopyroxenes in carbonatites and silicocarbonatites are not considered as xenocrysts derived from the nepheline syenites, but likely formed because of a local increase of silica activity in the carbonatite magma due to contamination processes. A similar origin is assumed for associated mica and for amphibole found in one carbonatite sample (ON028). While the major element compositions of clinopyroxene in ON038 and ON027 largely overlap (Fig. 7a), they show clear differences in their Zr content, and less so in Ti contents (Fig. 7b, c). We attribute these differences to contamination with different host rocks (nepheline syenites and granitic basement rocks, respectively).

Further evidence for local contamination is preserved in apatite compositions from clinopyroxene-bearing carbonatite ON038 and another carbonatite (ON021) that was sampled next to a syenite raft (Fig. 1b). In both samples, apatites show elevated Si contents, reaching similar levels as those from syenites and nepheline syenites (Fig. 8c). In comparison, apatite in carbonatite sample ON031 from the direct contact with a fenitized syenite has elevated Na contents, but is relatively low in Si (Fig. 8c, d). Apatite from an amphibole-bearing dolomite carbonatite (ON028) is exceptionally Sr-rich (Fig. 8b), which is either an effect of Sr-enrichment during evolution of the carbonatite magma, or alternatively indicates a hydrothermal origin. The latter would be in accordance with their yellow to orange CL color as opposed to violet blue typical of magmatic apatite from the investigated carbonatites.

5.1.2. Fenitization

The investigated fenites are characterized by green clinopyroxene (Fig. 7a), albite, and the strong alteration of alkali feldspar. Clinopyroxene from fenites is mostly fibrous and crystallized along veins (Fig. 6d) or replaced precursor minerals (e.g. quartz, mica; Fig. 6d, g), suggesting the involvement of a fenitizing fluid.

Irrespective of the protolith, two types of fenites can be distinguished, one containing carbonate – albite – microcline ± apatite ± sodic clinopyroxene assemblages in between large, very altered alkali feldspar (proximal fenites; ON010B, ON023; Fig. 6c), and the second one crystallized both sodic clinopyroxene and sodic amphibole in veins and between grain boundaries (distal fenites; ON029, fenite part of the sample ON031, ON033; Fig. 6g). Compared to clinopyroxene from nepheline syenites and carbonatites, clinopyroxenes from both fenite types show elevated Ti contents, with the highest values observed in the distal ones. This indicates significant Ti-mobility in the fenitizing fluids. Additionally, distal fenites contain quartz, and show a larger range in clinopyroxene compositions than the proximal ones (distal – $Aeg_{54-96}Di_{0-17}Hed_{0-16}$, proximal – $Aeg_{69-91}Di_{0-10}Hed_{0-7}$; Fig. 7a), which in majority contain near endmember aegirine. Since fenitization is a multi-stage process related to either carbonatite or alkaline silicate rocks, the fluid evolves in space and time, exchanging elements with the host rock depending on chemical differences (e.g. Elliott et al., 2018). This could explain the differences observed in proximal and distal fenites (difference in mineral assemblages and in clinopyroxene mineral chemistry), but more precise statements about the exact source of the fenitizing fluids, one likely from the carbonatite, but potentially also an earlier one from alkaline silicate rocks, cannot be made without additional data.

5.2. Two distinct episodes of magmatic activity in the Kalkfeld group

Our apatite ages are always significantly younger than those for titanite or zircon in the same sample, which can only be partly explained by much higher closure temperatures for zircon (~900 °C) and titanite (~700 °C) than for apatite (~450 °C; Cherniak et al., 1991; Cherniak,

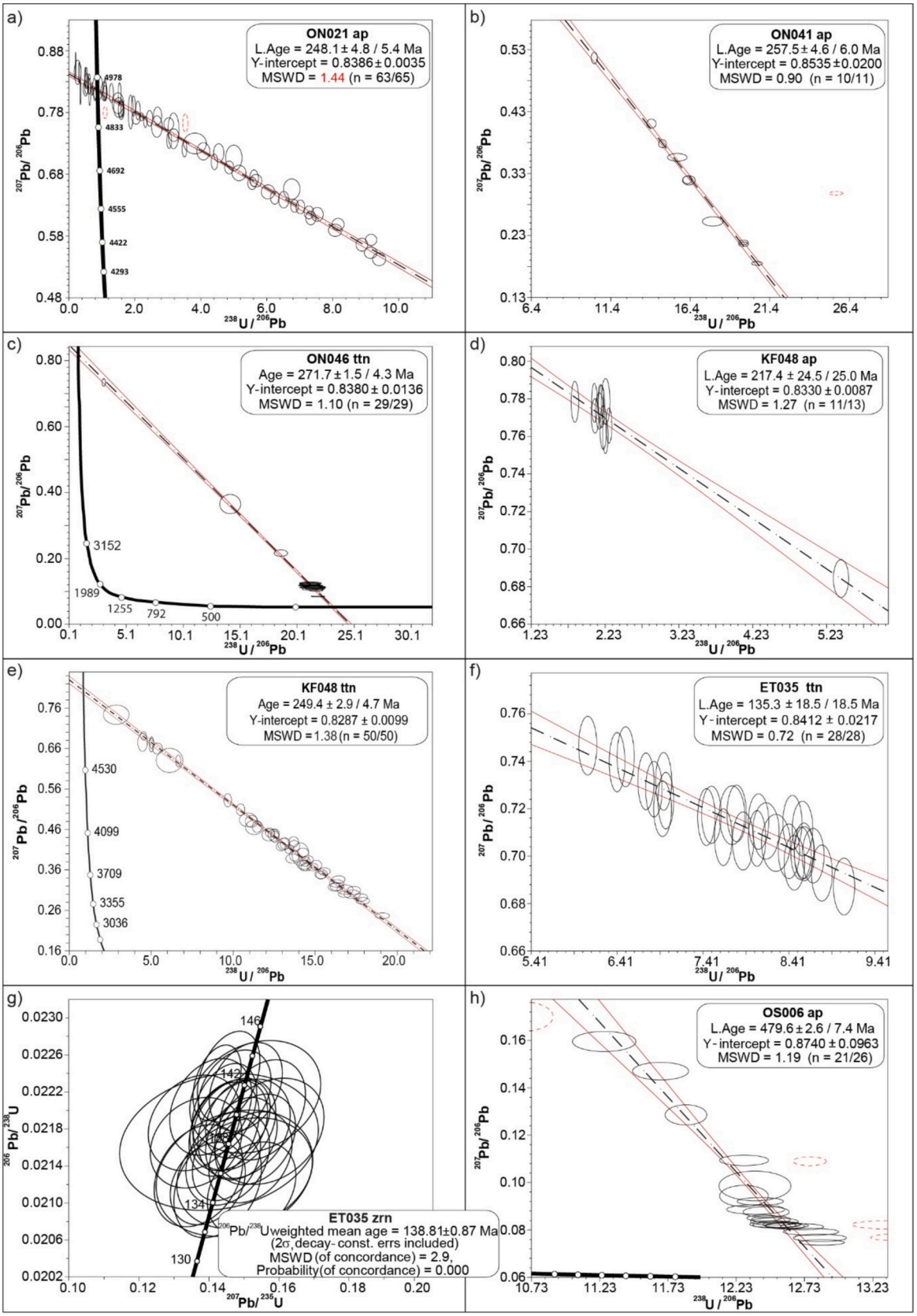

Fig. 10. Diagrams showing U-Pb ages of apatite, zircon and titanite from Ondurakorume (a – c), Kalkfeld (d, e), Etaneno (f, g) and Osongombo (h) dated by LA-SF-ICPMS, with error ellipses plotted as 2σ.

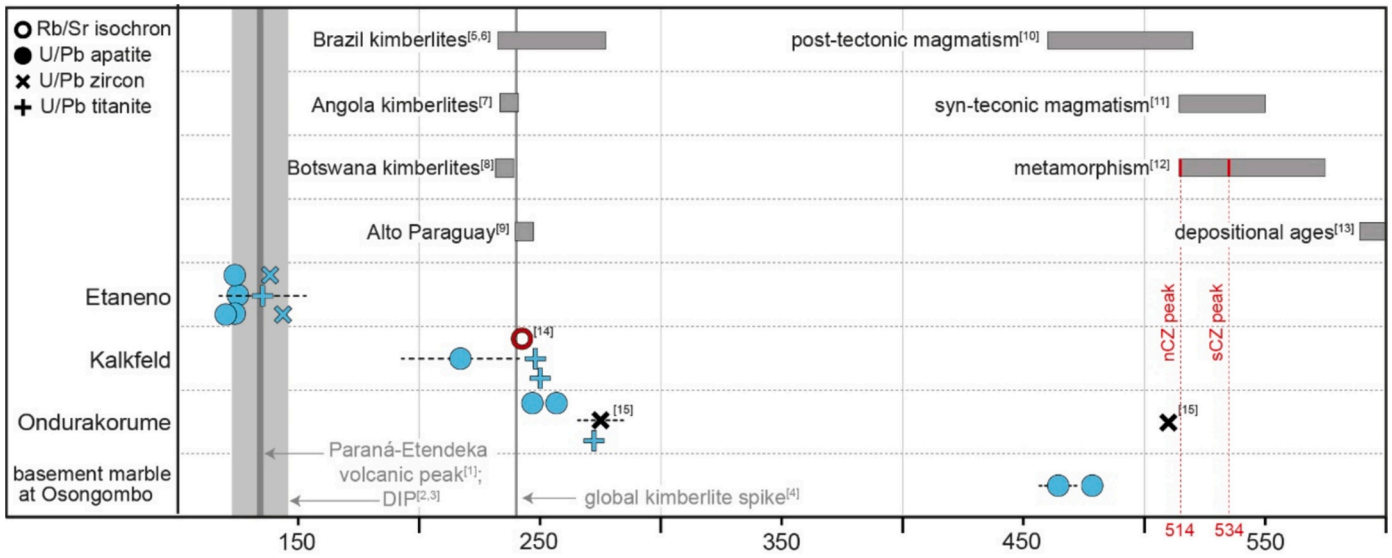

Fig. 11. Age distribution of major events thought to be related to, or have played a role in the formation of the complexes of the Kalkfeld group. The oldest recorded ages from the basement marbles at Osongombo coincide with post-tectonic (post Pan-African orogeny) magmatism, while Permo-Triassic ages recorded on Ondurakorume and Kalkfeld coincide with the global kimberlite spike around 240 Ma (see references below). This clearly shows these occurrences are not related to the early Cretaceous Paraná-Etendeka volcanism and related alkaline and carbonatitic complexes of the Damara Igneous Province (DIP), unlike Etaneno, which falls into the age range of the DIP. nCZ – North Central Zone (of which the Kalkfeld groups is a prat of), sCZ – South Central Zone. Blue symbols represent age data from this contribution, while red and black are two ages from the literature. References used in the figure: [1] Gomes and Vasconcelos (2021), [2] Müller, 1996, [3] Milner et al. (1995), [4] Tappe et al. (2018), [5] Masun and Scott Smith (2008), [6] Hunt et al. (2009), [7] Jelsma et al. (2013), [8] Honda et al. (2011), [9] Velázquez et al. (1996), [10] Toé et al. (2013), [11] Johnson et al. (2006), [12] Miller (2008), [13] Nascimento et al. (2017), [14] Kramm et al. (2017), [15] Sun et al. (2024). For interpretation of the references to color, the reader is referred to the web version of this article.

1993; Cherniak and Watson, 2001), assuming similar grain sizes. However, age differences of up to 30 Ma would imply unrealistically slow cooling rates of <15°/Ma. Still, slower cooling rates can be caused by tectonic movements and/or simultaneous or subsequent magmatism and fluid activity. On the other hand, there is an increasing body of evidence, that there may exist an intrinsic problem with U-Pb-dating of apatite, as more and more studies show consistently younger apatite than zircon or titanite ages from the same samples/complexes, not always explainable by a system reset (e.g. Gawęda et al., 2015; Marfin et al., 2021; Le Bras et al., 2022; Morrison et al., 2022). Furthermore, hydrothermal fluids may cause Pb loss in the apatite grains, which would explain the larger uncertainties in the acquired age data (Chew and Spikings, 2021). Without going into more detail (as this is not the main topic of this contribution), we simply state that our apatite ages (as many ages from the literature) may be too young, but they still fall into broadly the same range as the zircon and titanite ages and they show the same distinction between the complexes.

Our age data for Etaneno are within error of the recorded age range for the DIP (minimum recorded age ~123 Ma for Okanyenya; Milner et al., 1993; maximum recorded age ~144 Ma for Brandberg; Müller, 1996). Furthermore, the Permo-Triassic ages for Ondurakorume and Kalkfeld alkaline-silicate rocks, and additionally the Ondurakorume carbonatites (Table 6, Fig. 11) confirm recent results of Kramm et al. (2017) and Sun et al. (2024). The younger apatite ages obtained on Etaneno and Ondurakorume could indeed represent either cooling or reset ages caused by the subsequent magmatic activity in the close vicinity – the intrusions of DIP complexes along with Paraná-Etendeka volcanics for Etaneno, and the intrusion of the slightly younger Kalkfeld complex for Ondurakorume. However, the apatite age from Kalkfeld, along with its large error cannot be explained by a similar process and is therefore considered problematic and, for the time being, is difficult to interpret.

Permo-Triassic magmatism is not a common feature in southern Africa, but besides Kalkfeld and Ondurakorume, other Permo-Triassic igneous rocks from both sides of the Atlantic are known: kimberlites from Botswana (Jwaneng) and Angola (Lubia) have ages of 235 ± 4 Ma and 239–236 Ma (Honda et al., 2011; Jelsma et al., 2013), respectively, and several kimberlites in Brazil (Pimento Bueno field) show ages between 232 ± 2.3 Ma (Carolina-1) and 268 ± 9 Ma (Concord-1; Masun and Scott Smith, 2008; Hunt et al., 2009; Felgate, 2014). Furthermore, evolved (nepheline) syenites from the Alto Paraguay alkaline province (southeast of the Pimento Bueno kimberlite field) have ages of 245–240 Ma (Velázquez et al., 1996; Gomes et al., 2023). Kimberlites are, like other alkaline rocks and carbonatites, excellent markers for reconstructing paleotectonics, as they are often related to rifting, faulting, or reactivation of existing crustal weaknesses (Burke et al., 2003). In line with the recorded global kimberlite spike around 240 Ma (Tappe et al., 2018), the emplacement of the mentioned occurrences has been related to extension during initial rifting associated with the breakup of Pangea creating preferred pathways for their ascent (Comin-Chiaramonti et al., 2007; Honda et al., 2011; Jelsma et al., 2013; Campeny et al., 2014; Foulger, 2018; Almeida et al., 2024). Similarly, reactivation of Pan African shear zones has been suggested as causative for the formation of the Kalkfeld and Ondurakorume complexes (Kramm et al., 2017; Sun et al., 2024). Thus, the commonly used Tristan Plume formation model for the Early Cretaceous DIP complexes (Milner and Le Roex, 1996; Le Roex and Lanyon, 1998; Trumbull et al., 2000) clearly cannot explain their formation, as they are much older than the neighboring Etaneno complex.

The Ordovician ages of the basement marbles of roughly 480–465 Ma presented here postdates peak metamorphic conditions in the nCZ (about 514 Ma, Miller, 2008), but overlaps with *syn-* to post-tectonic magmatism (520–460 Ma, Toé et al., 2013; Miller, 2008; Fig. 11). Similarly, somewhat older ages (510 ± 5 Ma) are derived from zircons from a nephelinite syenite of Ondurakorume, and these have been interpreted to derive from Pan-African basement rocks (Sun et al., 2024).

6. Conclusions

The Ondurakorume carbonatite complex provides insights into the diverse interaction processes between alkaline silicate rocks and carbonatites: (I) Based on interstitial late-magmatic calcite with burbankite or carbocernaite inclusions and replacement of baddeleyite by zircon, we suggest that the partly solidified syenite crystal mush was locally infiltrated by carbonatitic melt. (II) Conversely, the presence of clinopyroxene, mica, and amphibole in some carbonatites and silicocarbonatites, along with compositional features of clinopyroxene and apatite in these samples, indicate interaction of the carbonatite magma with nepheline syenites and granitic basement rocks. (III) The emplacement of the carbonatite body induced fenitization, with mineralogical and chemical variations reflecting the spatial evolution of the fluid. Proximal fenites contain carbonate – albite – microcline ± apatite ± aegirine-augite pockets, while distal fenites show veined and grain boundary crystallization of aegirine-rich clinopyroxene and sodic amphibole.

Despite being spatially closely associated and consisting of similar alkaline-carbonatitic rocks, the Etaneno, Kalkfeld and Ondurakorume complexes did not all form during Early Cretaceous magmatism and are not genetically related to each other, but successively used local crustal weakness zones. While Etaneno exhibits a typical Early Cretaceous DIP age, Kalkfeld and Ondurakorume were already intruded during the Permo-Triassic as a consequence of initial the rifting associated with the breakup of Pangea. Ordovician ages obtained on the Damara marbles at Osongombo is unlikely to be related to the carbonatite intrusions, and rather suggest a metamorphic or post-tectonic cooling age.

Supplementary data to this article can be found online at https://doi.org/10.1016/j.chemer.2025.126287.

CRediT authorship contribution statement

Andreja Ladisic: Writing – review & editing, Writing – original draft, Visualization, Investigation, Conceptualization. **Michael A.W. Marks:** Writing – review & editing, Supervision, Project administration, Conceptualization. **Benjamin F. Walter:** Writing – review & editing, Supervision, Project administration, Funding acquisition, Conceptualization. **R. Johannes Giebel:** Writing – review & editing, Conceptualization. **Aratz Beranoaguirre:** Writing – original draft, Formal analysis. **Gregor Markl:** Writing – review & editing, Supervision, Project administration, Funding acquisition, Conceptualization.

Funding

This work was funded by the German Research Foundation (DFG) [grants WA 3116/3-1 and MA 2135/26].

Declaration of competing interest

The authors declare that they have no known competing financial interests or personal relationships that could have appeared to influence the work reported in this paper.

Acknowledgements

We extend our gratitude to the handling editor Tomáš Magna and two anonymous reviewers whose comments greatly improved this contribution. Anna Nguno (Ministry of Mines and Energy, Namibia) is thankfully acknowledged for help with some of the logistical matters, and Inka van der Bijl (Geological Society of Namibia) for providing us with the opportunity to present our ongoing research to the Namibian geological community. We would like to thank Pete Siegfried for all the help with logistical matters and to Burger Oelofsen for granting us access to his farm, which enabled sample collection. We express our gratitude to MiĘKiNiA Lab for thin section preparation. Special thanks to Sebastian Staude for all assistance and help acquiring EPMA data. Furthermore, we acknowledge Aurelia Zirner for her contribution in digitizing the maps in QGIS. Big thank you goes to Thomas Binder and Tobias Fußwinkel for the help with Li analyses.

References

Almeida, V.V., Ribeiro, B.V., Rodrigues, J.B., Cawood, P.A., Neto, I.C., Silveira, F.V., Faleiros, F.M., Kirscher, U., 2024. Linking kimberlite magmatism in the Brazilian Platform with Pangea break-up events using in situ Rb-Sr in phlogopite. Lithos 468–469, 107486. https://doi.org/10.1016/j.lithos.2023.107486.

Andersen, T., Carr, P., Erambert, M., 2012. Late-magmatic mineral assemblages with siderite and zirconian pyroxene and amphibole in the anorogenic Mt Gibraltar microsyenite, New South Wales, Australia, and their petrological implications. Lithos 151, 46–56. https://doi.org/10.1016/j.lithos.2011.09.012.

Anenburg, M., Mavrogenes, J.A., 2018. Carbonatitic versus hydrothermal origin for fluorapatite REE-Th deposits: Experimental study of REE transport and crustal "antiskarn" metasomatism. Am. J. Sci. 318, 335–366. https://doi.org/10.2475/03.2018.03.

Anenburg, M., Walters, J.B., 2024. Metasomatic ijolite, glimmerite, silicocarbonatite, and antiskarn formation: carbonatite and silicate phase equilibria in the system Na_2O–CaO–K_2O–FeO–MgO–Al_2O_3–SiO_2–H_2O–O_2–CO_2. Contrib. Mineral. Petrol. 179, 40. https://doi.org/10.1007/s00410-024-02109-0.

Anenburg, M., Broom-Fendley, S., Chen, W., 2021. Formation of Rare Earth Deposits in Carbonatites. Elements 17 (5), 327–332. https://doi.org/10.2138/gselements.17.5.327.

Beranoaguirre, A., Vasiliev, I., Gerdes, A., 2022. In situ LA-ICPMS U–Pb dating of sulfates: applicability of carbonate reference materials as matrix-matched standards. Geochronology 4, 601–616. https://doi.org/10.5194/gchron-4-601-2022.

Bouabdellah, M., Boukirou, W., Jébrak, M., Bigot, F., Yans, J., Mouttaqi, A., El Gadarri, M., Errami, A., Levresse, G., 2022. Discovery of antiskarn-hosted strategic metal mineralization in the Upper Cretaceous Twihinate carbonatite intrusion (West African Craton Margin, Moroccan Sahara). Ore Geol. Rev. 149, 105105. https://doi.org/10.1016/j.oregeorev.2022.105105.

Bühn, B., 2008. The role of the volatile phase for REE and Y fractionation in low-silica carbonate magmas: implications from natural carbonatites, Namibia. Miner. Petrol. 92, 453–470. https://doi.org/10.1007/s00710-007-0214-4.

Bühn, B., Trumbull, R.B., 2003. Comparison of petrogenetic signatures between mantle-derived alkali silicate intrusives with and without associated carbonatite, Namibia. Lithos 66 (3–4), 201–221. https://doi.org/10.1016/S0024-4937(02)00220-7.

Bühn, B., Wall, F., Le Bas, M.J., 2001. Rare-earth element systematics of carbonatitic fluorapatites, and their significance for carbonatite magma evolution. Contrib. Mineral. Petrol. 141, 572–591. https://doi.org/10.1007/s00410010026.

Burke, K., Ashwal, L.D., Webb, S.J., 2003. New way to map old sutures using deformed alkaline rocks and carbonatites. Geology 31 (5), 391–394. https://doi.org/10.1130/0091-7613(2003)031<0391:NWTMOS>2.0.CO;2.

Campeny, M., Mangas, J., Melgarejo, J.C., Bambi, A., Alfonso, P., Gernon, T., Manuel, J., 2014. The Catanda extrusive carbonatites (Kwanza Sul, Angola): an example of explosive carbonatitic volcanism. Bull. Volcanol. 76 (818), 1–15. https://doi.org/10.1007/s00445-014-0818-6.

Chakhmouradian, A.R., 2006. High-field-strength elements in carbonatitic rocks: Geochemistry, crystal chemistry and significance for constraining the sources of carbonatites. Chem. Geol. 235 (1–2), 138–160. https://doi.org/10.1016/j.chemgeo.2006.06.008.

Chakhmouradian, A., Dahlgren, S., 2021. Primary inclusions of burbankite in carbonatites from the Fen complex, southern Norway. Miner. Petrol. 115, 161–171. https://doi.org/10.1007/s00710-021-00736-0.

Cherniak, D.J., 1993. Lead diffusion in titanite and preliminary results on the effects of radiation damage on Pb transport. Chem. Geol. 110 (1–3), 177–194. https://doi.org/10.1016/0009-2541(93)90253-F.

Cherniak, D.J., Watson, E.B., 2001. Pb diffusion in zircon. Chem. Geol. 172 (1–2), 5–24. https://doi.org/10.1016/S0009-2541(00)00233-3.

Cherniak, D.J., Lanford, W.A., Ryerson, F.J., 1991. Lead diffusion in apatite and zircon using ion implantation and Rutherford backscattering techniques. Geochim. Cosmochim. Ac. 55 (6), 1663–1673. https://doi.org/10.1016/0016-7037(91)90137-T.

Chew, D., Spikings, R.A., 2021. Apatite U-Pb thermochronology: a review. Minerals 11 (10), 1095. https://doi.org/10.3390/min11101095.

Comin-Chiaramonti, P., Marzoli, A., Gomes, C.B., Milan, A., Riccomini, C., Velázquez, V. F., Mantovani, M.M.S., Renne, P., Tassinari, C.C.G., Vasconcelos, P.M., 2007. The origin of post-Paleozoic magmatism in eastern Paraguay. In Foulger, G.R., Jurdy, D. M., plates, eds., Plates, plumes and planetary processes. Geol. Soc. Am. Spec. Paper 430, 603–633. https://doi.org/10.1130/2007.2430(29).

Comin-Chiaramonti, P., De Min, A., Girardi, V.A.V., Ruberti, E., 2011. Post-Paleozoic magmatism in Angola and Namibia: a review. In Beccaluva, L., Bianchini, G., Wilson, M., eds., Volcanism and Evolution of the African Lithosphere. Geol. Soc. Am. Spec. Paper 478, 223–247. https://doi.org/10.1130/2011.2478(12).

Cooper, A.F., Paterson, L.A., Reid, D.L., 1995. Lithium in carbonatites—consequence of an enriched mantle source? Mineral. Mag. 59 (396), 401–408. https://doi.org/10.1016/j.lithos.2015.11.035.

Cooper, A.F., Palin, J.M., Collins, A.K., 2016. Fenitization of metabasic rocks by ferrocarbonatites at Haast River, New Zealand. Lithos 244, 109–121.

Droop, G.T.R., 1987. A general equation for estimating Fe3+ concentrations in ferromagnesian silicates and oxides from microprobe analyses, using stoichiometric

criteria. Mineral. Mag. 51 (361), 431–435. https://doi.org/10.1180/minmag.1987.051.361.10.
Elliott, H.A.L., Wall, F., Chakhmouradian, A.R., Siegfried, P.R., Dahlgren, S., Weatherley, S., Finch, A.A., Marks, M.A.W., Dowman, E., Deady, E., 2018. Fenites associated with carbonatite complexes: A review. Ore Geol. Rev. 93, 38–59. https://doi.org/10.1016/j.oregeorev.2017.12.003.
Ewart, A., Marsh, J.S., Milner, S.C., Duncan, A.R., Kamber, B.S., Armstrong, R.A., 2004. Petrology and Geochemistry of Early Cretaceous Bimodal Continental Flood Volcanism of the NW Etendeka, Namibia. Part 1: Introduction, Mafic Lavas and Re-evaluation of Mantle Source Components. J. Petrol. 45 (1), 59–105. https://doi.org/10.1093/petrology/egg083.
Felgate, M., 2014. The petrogenesis of Brazilian kimberlites and kamafugites intruded along the 125° lineament: Improved geochemical and geochronological constraints on magmatism in Rondonia and the Alto Paranaiba Igneous Province. Doctoral dissertation. The University of Melbourne.
Foulger, G.R., 2018. Origin of the South Atlantic igneous province. J. Volcanol. Geoth. Res. 355, 2–20. https://doi.org/10.1016/j.jvolgeores.2017.09.004.
Gawęda, A., Gauert, C., Szopa, K., Chew, D., Giebel, J., 2015. Palaeoproterozoic post-magmatic cooling of the Phalaborwa Complex, South Africa, constrained by U-Pb apatite dating. Mineralogia – Special Papers 44, 37.
Gerdes, A., Zeh, A., 2006. Combined U-Pb and Hf isotope LA-(MC-)ICP-MS analyses of detrital zircons: comparison with SHRIMP and new constraints for the provenance and age of an Armorican metasediment in Central Germany. Earth Planet. Sc. Lett. 249, 47–61. https://doi.org/10.1016/j.epsl.2006.06.039.
Gerdes, A., Zeh, A., 2009. Zircon formation versus zircon alteration — new insights from combined U-Pb and Lu-Hf in-situ LA-ICP-MS analyses, and consequences for the interpretation of Archean zircon from the Central Zone of the Limpopo Belt. Chem. Geol. 261 (3–4), 230–243. https://doi.org/10.1016/j.chemgeo.2008.03.005.
Giebel, R.J., Parsapoor, A., Walter, B.F., Braunger, S., Marks, M.A.W., Wenzel, T., Markl, G., 2019. Evidence for magma–wall rock interaction in carbonatites from the kaiserstuhl volcanic complex (Southwest Germany). J. Petrol. 60 (6), 1163–1194. https://doi.org/10.1093/petrology/egz028.
Gittins, J., Mitchell, R.H., 2023. The genesis of calcite and dolomite carbonatite-forming magma by liquid immiscibility: a critical appraisal. Geol. Mag. 160 (8), 1463–1480. https://doi.org/10.1017/S001675682300050X.
Gomes, A.S., Vasconcelos, P.M., 2021. Geochronology of the Paraná-Etendeka large igneous province. Earth Sci. Rev. 220, 103716. https://doi.org/10.1016/j.earscirev.2021.103716.
Gomes, C.B., Comin-Chiaramonti, P., Azzone, R.G., Ruberti, E., Rojas, G.E., 2018. Cretaceous carbonatites of the southeastern Brazilian Platform: a review. Braz. J. Geol. 48 (2), 317–345. https://doi.org/10.1590/2317-4889201820170123.
Gomes, C.B., Comin-Chiaramonti, P., Velázquez, V.F., Riccomini, C., 2023. The Alto Paraguay alkaline province at the border of Brazil and Paraguay: General features. J. South Am. Earth Sci. 130, 104535. https://doi.org/10.1016/j.jsames.2023.104535.
Honda, M., Phillips, D., Harris, J.W., Matsumoto, T., 2011. He, Ne and Ar in peridotitic and eclogitic paragenesis diamonds from the Jwaneng kimberlite, Botswana—implications for mantle evolution and diamond formation ages. Earth Planet. Sc. Lett. 301 (1–2), 43–51. https://doi.org/10.1016/j.epsl.2010.10.008.
Horstwood, M.S.A., Košler, J., Gehrels, G., Jackson, S.E., McLean, N.M., Paton, C., Pearson, N.J., Sircombe, K., Sylvester, P., Vermeesch, P., Bowring, J.F., 2016. Community-Derived Standards for LA-ICP-MS U-(Th-)Pb Geochronology - Uncertainty Propagation, Age Interpretation and Data Reporting. Geostand. Geoanal. Res. 40, 311–332. https://doi.org/10.1111/j.1751-908X.2016.00379.x.
Hunt, L., Stachel, T., Morton, R., Grütter, H., Creaser, R.A., 2009. The Carolina kimberlite, Brazil — Insights into an unconventional diamond deposit. Lithos 112, 843–851. https://doi.org/10.1016/j.lithos.2009.04.018.
Jackson, S.E., Pearson, N.J., Griffin, W.L., Belousova, E.A., 2004. The application of laser ablation-inductively coupled plasma-mass spectrometry to in situ U–Pb zircon geochronology. Chem. Geol. 211, 47–69. https://doi.org/10.1016/j.chemgeo.2004.06.017.
Jelsma, H., Krishnan, U., Perritt, S., Preston, R., Winter, F., Lemotlo, L., van der Linde, G., Armstrong, R., Phillips, D., Joy, S., Costa, J., Facatino, M., Posser, M., Kumar, M., Wallace, C., Chinn, I., Henning, A., 2013. Kimberlites from Central Angola: A Case Study of Exploration Findings. In: Pearson, D.G., Grütter, H.S., Harris, J.W., Kjarsgaard, B.A., O'Brien, H., Rao, C.N.V., Sparks, S. (Eds.), Proceedings of 10th International Kimberlite Conference, vol. 2. Springer, New Delhi, pp. 173–190. https://doi.org/10.1007/978-81-322-1173-0_12.
Jochum, K.P., Weis, U., Stoll, B., Kuzmin, D., Yang, Q., Raczek, I., Jacob, D.E., Stracke, A., Birbaum, K., Frick, D.A., Günther, D., Enzweiler, J., 2011. Determination of reference values for NIST SRM 610–617 glasses following ISO guidelines. Geostand. Geoanal. Res. 35, 97–429. https://doi.org/10.1111/j.1751-908X.2011.00120.x.
Johnson, S.D., Poujol, M., Kisters, A.F.M., 2006. Constraining the timing and migration of collisional tectonics in the Damara Belt, Namibia: U-Pb zircon ages for the syntectonic Salem-type Stinkbank granite. S. Afr. J. Geol. 109 (4), 611–624. https://doi.org/10.2113/gssajg.109.4.611.
Jones, A.P., Peckett, A., 1981. Zirconium-bearing aegirines from Motzfeldt, South Greenland. Contrib. Mineral. Petr. 75, 251–255. https://doi.org/10.1007/BF01166764.
Jones, A.P., Genge, M., Carmody, L., 2013. Carbonate Melts and Carbonatites. Rev. Mineral. Geochem. 75 (1), 289–322. https://doi.org/10.2138/rmg.2013.75.10.
Kramm, U., Körner, T., Kittel, M., Baier, H., Sindern, S., 2017. Triassic emplacement age of the Kalkfeld complex, NW Namibia: implications for carbonatite magmatism and its relationship to the Tristan Plume. Int. J. Earth Sci. (Geol. Rundsch) 106, 2797–2813. https://doi.org/10.1007/s00531-017-1460-2.
Lana, C., Gonçalves, G.O., Mazoz, A., Buick, I., Kamo, S., Scholz, R., Wang, H., Moreira, H., Babinski, M., Queiroga, G., 2021. Assessing the U-Pb, Sm-Nd and Sr-Sr Isotopic Compositions of the Sume Apatite as a Reference Material for LA-ICP-MS Analysis. Geostand. Geoanal. Res. 46, 71–95. https://doi.org/10.1111/ggr.12413.
Le Bas, M.J., 2008. Fenites associated with carbonatites. Can. Mineral. 46 (4), 915–932. https://doi.org/10.3749/canmin.46.4.915.
Le Bras, L.Y., Milani, L., Bolhar, R., O'Sullivan, G., 2022. Applying U-Pb chronometry and trace element geochemistry of apatite to carbonatite-phoscorite complexes – as exemplified by the 2.06 Ga Phalaborwa Complex, South Africa. S. Afr. J. Geol. 125 (2), 179–190. https://doi.org/10.25131/sajg.125.0015.
Le Maitre, R.W., Streckeisen, A., Zanettin, B., Le Bas, M.J., Bonin, B., Bateman, P., Bellieni, G., Dudek, A., Efremov, S., Keller, J., Lameyre, J., Sabine, P.A., Schmid, R., Sorensen, H., Woolley, A.R., 2002. Igneous Rocks: A Classification and Glossary of Terms, 2nd edn. Cambridge University Press, Cambridge. https://doi.org/10.1017/CBO97 80511 535581.
Le Roex, A.P., Lanyon, R., 1998. Isotope and trace element geochemistry of Cretaceous Damaraland lamprophyres and carbonatites, northwestern Namibia: Evidence for plume—lithosphere interactions. J. Petrol. 39, 1117–1146. https://doi.org/10.1093/petroj/39.6.1117.
Locock, A.J., 2014. An Excel spreadsheet to classify chemical analyses of amphiboles following the IMA 2012 recommendations. Comput. Geosci. 62, 1–11. https://doi.org/10.1016/j.cageo.2013.09.011.
Ludwig, K.R., 2012. User's Manual for Isoplot Version 3.75-4.15: A Geochronological Toolkit for Microsoft Excel. Berkeley Geochronological Center Special Publication, 5.
Mann, U., Marks, M.A.W., Markl, G., 2006. Influence of oxygen fugacity on mineral compositions in peralkaline melts: The Katzenbuckel volcano, Southwest Germany. Lithos 91 (1–4), 262–285. https://doi.org/10.1016/j.lithos.2005.09.004.
Marfin, A.E., Radomskaya, T.A., Ivanov, A.V., Kamenetsky, V.S., Kamenetsky, M.B., Yakich, T.Y., Gertner, I.F., Kamo, S.F., Ernst, R.E., Bryanskiy, N.V., Glazunov, O.M., Belozerova, O.Y., 2021. U–Pb dating of Apatite, Titanite and Zircon of the Kingash Mafic–Ultramafic Massif, Kan Terrane, Siberia: from Rodinia Break-up to the Reunion with the Siberian Craton. J. Petrol. 62 (9), 1–16. https://doi.org/10.1093/petrology/egab049.
Martin, R.F., 2007. Amphiboles in the igneous environment. Rev. Mineral. Geochem. 67 (1), 323–358. https://doi.org/10.2138/rmg.2007.67.9.
Masun, K.M., Scott Smith, B.H., 2008. The Pimenta Bueno kimberlite field, Rondônia, Brazil: Tuffisitic kimberlite and transitional textures. J. Volcanol. Geoth. Res. 174 (1–3), 81–89. https://doi.org/10.1016/j.jvolgeores.2007.12.043.
Mazoz, A., Gonçalves, G.O., Lana, C., Buick, I.S., Corfu, F., Kamo, S.L., Wang, H., Yang, Y. H., Scholz, R., Queiroga, G., Martins, L., Schannor, M., Abreu, A.T., Babinski, M., Ventura, R., Peixoto, E., 2022. Khan River and Bear Lake: Two natural titanite reference materials for high-spatial resolution U-Pb microanalysis. Geostand. Geoanal. Res. 46, 701–733. https://doi.org/10.1111/ggr.12444.
McDowell, F.W., McIntosh, W.C., Farley, K.A., 2005. A precise ^{40}Ar-^{39}Ar reference age for the Durango apatite(U–Th)/He and fission-track dating standard. Chem. Geol. 214, 249–263. https://doi.org/10.1016/j.chemgeo.2004.10.002.
Miller, R.M., 2008. Neoproterozoic and early Palaeozoic rocks of the Damara Orogen. In: Miller, R.M. (Ed.), The geology of Namibia. Geol. Surv. Namibia, 2, pp. 13.1–13.410.
Milner, S.C., Le Roex, A.P., 1996. Isotope characteristics of the Okenyenya igneous complex, northwestern Namibia: constraints on the composition of the early Tristan plume and the origin of the EM I mantle component. Earth. Plan. Sci. Lett. 141, 277–291. https://doi.org/10.1016/0012-821X(96)00074-X.
Milner, S.C., Le Roex, A.P., Watkins, R.T., 1993. Rb-Sr age determinations of rocks from the Okenyenya igneous complex, northwestern Namibia. Geol. Mag. 130 (3), 335–343. https://doi.org/10.1017/S001675680002001X.
Milner, S.C., Le Roex, A.P., O'Connor, J.M., 1995. Age of Mesozoic igneous rocks in northwestern Namibia, and their relationship to continental breakup. J. Geol. Soc. Lond. 152, 97–104. https://doi.org/10.1144/gsjgs.152.1.0097.
Mitchell, R.H., 2005. Carbonatites and carbonatites and carbonatites. Can. Mineral. 43 (6), 2049–2068. https://doi.org/10.2113/gscanmin.43.6.2049.
Morogan, V., Woolley, A.R., 1988. Fenitization at the Alnö carbonatite complex, Sweden; distribution, mineralogy and genesis. Contrib. Miner. Petrol. 100, 169–182. https://doi.org/10.1007/BF00373583.
Morrison, J.L., Kirkland, C.L., Fiorentini, M., Beresford, S., Polito, P., 2022. An apatite to unravel petrogenic processes of the Nova-Bollinger Ni-Cu magmatic sulfide deposit, Western Australia. Precambrian Res. 369, 106524. https://doi.org/10.1016/j.precamres.2021.106524.
Müller, B., 1996. Ring complexes of the Damaraland alkaline province, Namibia, in the light of geochemistry and Rb–Sr, U-Pb, Pb-Pb isotopes. Doctoral dissertation. ETH Zürich.
Nascimento, D.B., Schmitt, R.S., Ribeiro, A., Trouw, R.A.J., Passchier, C.W., Basei, M.A. S., 2017. Depositional ages and provenance of the Neoproterozoic Damara Supergroup (northwest Namibia): Implications for the Angola-Congo and Kalahari cratons connection. Gondw. Res. 52, 153–171. https://doi.org/10.1016/j.gr.2017.09.006.
Nelson, D., Chivas, A.R., Chappell, B., McCulloch, M., 1988. Geochemical and isotopic systematics in carbonatites and implications for the evolution of ocean-island sources. Geochim. Cosmochim. Ac. 52, 1–17. https://doi.org/10.1016/0016-7037(88)90051-8.
Prins, P., 1978. The geochemical evolution of the alkaline and carbonatite complexes of the Damaraland igneous province, South West Africa. Doctoral dissertation. Stellenbosch University.
Santos, M.M., Lana, C., Scholz, R., Buick, I., Schmitz, M.D., Kamo, S.L., Gerdes, A., Corfu, F., Tapster, S., Lancaster, P., Storey, C.D., Basei, M.A., Tohver, E., Alkmim, A., Nalini, H., Krambrock, K., Fantini, C., Wiedenbeck, M., 2017. A New Appraisal of Sri Lankan BB Zircon as a Reference Material for LA-ICP-MS U-Pb Geochronology and

Lu-Hf Isotope Tracing. Geostand. Geoanal. Res. 41 (3), 335–358. https://doi.org/10.1111/ggr.12167.

Sláma, J., Košler, J., Condon, D.J., Crowley, J.L., Gerdes, A., Hanchar, J.M., Horstwood, M.S.A., Morris, G.A., Nasdala, L., Norberg, N., Schaltegger, U., Schoene, B., Tubrett, M.N., Whitehouse, M.J., 2008. Plešovice zircon — a new natural reference material for U–Pb and Hf isotopic microanalysis. Chem. Geol. 249 (1–2), 1–35. https://doi.org/10.1016/j.chemgeo.2007.11.005.

Sun, Y., Galli, A., Szymanowski, D., Guillong, M., Rosskopf, R., Simon, J., Shipandeni, A., Bachmann, O., 2024. High-precision zircon geochronology and geochemistry of evolved magmatic centres in the Paraná-Etendeka LIP: Temporal placement and tectono-magmatic origin of the Damaraland complexes, Namibia. Lithos 480–481, 107651. https://doi.org/10.1016/j.lithos.2024.107651.

Tappe, S., Smart, K., Torsvik, T., Massuyeau, M., de Wit, M., 2018. Geodynamics of kimberlites on a cooling Earth: Clues to plate tectonic evolution and deep volatile cycles. Earth Planet. Sc. Lett. 484, 1–14. https://doi.org/10.1016/j.epsl.2017.12.013.

Toé, W., Vanderhaeghe, O., André-Mayer, A.S., Feybesse, J.L., Milési, J.P., 2013. From migmatites to granites in the Pan-African Damara orogenic belt, Namibia. J. Afr. Earth Sci. 85, 62–74. https://doi.org/10.1016/j.jafrearsci.2013.04.009.

Trumbull, R.B., Emmermann, R., Bühn, B., Gerstenberger, H., Mingram, B., Schmitt, A., Volker, F., 2000. Insights on the genesis of the Cretaceous Damaraland igneous complexes in Namibia from a Nd- and Sr-isotopic perspective. Commun. Geol. Surv. Namibia 12, 313–324.

Trumbull, R.B., Bühn, B., Romer, R.L., Volker, F., 2003. The petrology of basanite—tephrite intrusions in the Erongo complex and implications for the plume origin of Cretaceous alkaline complexes in Namibia. J. Petrol. 44, 93–112. https://doi.org/10.1093/petrology/44.1.93.

Vasyukova, O.V., Williams-Jones, A.E., 2022. Carbonatite metasomatism, the key to unlocking the carbonatite-phoscorite-ultramafic rock paradox. Chem. Geol. 602, 120888. https://doi.org/10.1016/j.chemgeo.2022.120888.

Vasyukova, O., Kostyuk, A., Williams-Jones, A., 2022. Kovdor to Oldoinyo Lengai—The missing link in carbonatitic magma evolution. Geology 51 (1), 59–63. https://doi.org/10.1130/G50672.1.

Velázquez, V.F., Gomes, C.D., Teixeira, W., Comin-Chiaramonti, P., 1996. Contribution to the geochronology of the Permo-Triassic alkaline magmatism of the Alto Paraguay province. Braz. J. Geol. 26, 103–108. https://doi.org/10.25249/0375-7536.1996103108.

Verwoerd, W.J., 1967. The carbonatites of South Africa and South West Africa. Geol. Surv. S. Africa. Handbook 6, 452pp.

Verwoerd, W.J., Retief, E.A., Prins, P., 2000. The Etanenoberg alkaline complex, Namibia. Communs geol. Surv. Namibia 12, 291–300.

Voropaeva, D., Arzamastsev, A.A., Botcharnikov, R., Buhre, S., Gilbricht, S., Götze, J., Klemd, R., Schulz, B., Tichomirowa, M., 2024. LREE rich perovskite in antiskarn reactions - REE transfer from pyroxenites to carbonatites? Lithos 468–469, 107480. https://doi.org/10.1016/j.lithos.2023.107480.

Walter, B.F., Giebel, R.J., Steele-MacInnis, M., Marks, M.A.W., Kolb, J., Markl, G., 2021. Fluids associated with carbonatitic magmatism: A critical review and implications for carbonatite magma ascent. Earth Sci. Rev. 215, 103509. https://doi.org/10.1016/j.earscirev.2021.103509.

Woolley, A.R., Kjarsgaard, B.A., 2008. Paragenetic types of carbonatite as indicated by the diversity and relative abundances of associated silicate rocks: Evidence from a global database. Can. Mineral. 46 (4), 741–752. https://doi.org/10.3749/canmin.46.4.741.

Yaxley, G.M., Anenburg, M., Tappe, S., Decree, S., Guzmics, T., 2022. Carbonatites: Classification, Sources, Evolution, and Emplacement. Annu. Rev. Earth Pl. Sc. 50, 261–293. https://doi.org/10.1146/annurev-earth-032320-104243.